

A high-order implicit least square-based finite difference-finite volume method for incompressible flows on unstructured grids

Cite as: Phys. Fluids **33**, 053601 (2021); <https://doi.org/10.1063/5.0047192>

Submitted: 11 February 2021 . Accepted: 08 April 2021 . Published Online: 03 May 2021

 Y. Y. Liu (刘阳阳),  C. Shu (舒昌),  H. W. Zhang (张黄伟), and  L. M. Yang (杨锂铭)



View Online



Export Citation



CrossMark

ARTICLES YOU MAY BE INTERESTED IN

[Development of an immersed boundary-multiphase lattice Boltzmann flux solver with high density ratio for contact line dynamics](#)

Phys. Fluids **33**, 057101 (2021); <https://doi.org/10.1063/5.0043604>

[Three-dimensional high-order least square-based finite difference-finite volume method on unstructured grids](#)

Phys. Fluids **32**, 123604 (2020); <https://doi.org/10.1063/5.0032089>

[A high-fidelity numerical study on the propulsive performance of pitching flexible plates](#)

Phys. Fluids **33**, 051901 (2021); <https://doi.org/10.1063/5.0049217>

Physics of Fluids

SPECIAL TOPIC: Tribute to
Frank M. White on his 88th Anniversary

SUBMIT TODAY!



A high-order implicit least square-based finite difference-finite volume method for incompressible flows on unstructured grids

Cite as: Phys. Fluids **33**, 053601 (2021); doi: [10.1063/5.0047192](https://doi.org/10.1063/5.0047192)

Submitted: 11 February 2021 · Accepted: 8 April 2021 ·

Published Online: 3 May 2021



View Online



Export Citation



CrossMark

Y. Y. Liu (刘阳阳),¹  C. Shu (舒昌),^{1,a)}  H. W. Zhang (张黄伟),¹  and L. M. Yang (杨铿铭)² 

AFFILIATIONS

¹Department of Mechanical Engineering, National University of Singapore, 10 Kent Ridge Crescent, Singapore 119260

²Department of Aerodynamics, College of Aerospace Engineering, Nanjing University of Aeronautics and Astronautics, Yudao Street, Nanjing 210016, Jiangsu, China

^{a)}Author to whom correspondence should be addressed: mpeshuc@nus.edu.sg

ABSTRACT

In this study, a high-order implicit least squares-based finite difference-finite volume (ILSFD-FV) method with a lattice Boltzmann flux solver is presented for the simulation of two-dimensional incompressible flows on unstructured grids. In this method, a high-order polynomial based on Taylor series expansion is applied within each control cell, where the unknown spatial derivatives at each cell center are approximated by the least squares-based finite difference scheme. The volume integral of the high-order polynomial over the control cell results in a pre-multiplied coefficient matrix in the time-dependent term. This makes the high-order method be implicit in nature. With this feature, a high-order implicit Runge–Kutta time integration scheme, namely, the explicit first-stage singly diagonally implicit Runge–Kutta (ESDIRK) scheme, is applied to obtain the time-accurate solutions for flow problems. The non-linear system of equations arising from each ESDIRK stage except for the first explicit stage is solved by a dual time stepping approach. A matrix-free lower-upper symmetric Gauss–Seidel solver is then used to efficiently march the solution in the pseudo time. The present high-order ILSFD-FV method is verified and validated by both steady and unsteady 2D incompressible flow problems. Numerical results indicate that the developed implicit method outperforms its explicit counterpart in terms of the convergence property and computational efficiency. The speedup ratio of the computational effort is about 3–22.

Published under license by AIP Publishing. <https://doi.org/10.1063/5.0047192>

I. INTRODUCTION

High-order numerical methods have attracted great interest in studying turbulence, aeroacoustics, and many viscosity-dominated flows, such as boundary layer flows, vortical flows, shock-boundary layer interactions, and heat flux transfers. In comparison with low-order methods which have played an important role in engineering applications due to their robust and reliable characteristics, high-order methods become competitive since they can provide higher accuracy with similar cost. In addition, the desire to solve practical flow problems with complex geometries has prompted the development of high-order methods on unstructured grids.

In the past two decades, there have been various high-order methods on unstructured grids developed in the computational fluid dynamics (CFD) community and they are successfully applied to solve diverse flow problems. Representative ones are the high-order finite volume (FV) method,^{1–4} essentially non-oscillatory (ENO) and weighted essentially non-oscillatory (WENO) method,^{5–9} discontinuous Galerkin

(DG) method,^{10–16} spectral difference (SD) method,^{17,18} spectral volume (SV) method,^{19–23} and correction procedure via reconstruction (CPR) method.^{24,25} These methods all apply a high-order polynomial to approximate the solution function within each control cell. However, the respective technique for approximating the unknowns in the high-order polynomial is clearly distinctive. Specifically, the DG method increases the number of discrete equations to that of the unknowns by weighted integrations of governing equations over the control cell. After solving the resultant equation system, the unknowns can be approximated. The SV/SD method adopts a different technique, in which additional degrees of freedom are constituted by cell subdivision or solution point distributions in a proper manner inside each control cell. Based on the functional values at the subcells or solution points, a high-order polynomial in the control cell is established and then is applied to the subcell or solution point for discretization of governing equations. Apart from DG and SV/SD methods, one pioneering high-order finite volume method is k -exact method.²⁶ In this method, a modified Taylor

series expansion is applied to guarantee high-order solution approximation within each cell. To determine the unknowns, namely, the spatial derivatives at the cell center, the Taylor series expansion needs to be integrated over the current cell and its neighboring cells, respectively. Then, the unknowns can be calculated by solving the resultant equation system with the mean values of the solution function at the current cell and its neighboring cells.

Recently, Shu and his coworkers proposed a straightforward high-order FV method on the unstructured grid, called least squares-based finite difference-finite volume (LSFD-FV) method.²⁷ In the LSFD-FV method, a Taylor series expansion is applied within each control cell and this Taylor polynomial is used as the interpolation function directly to approximate the solution with required accuracy. The unknown spatial derivatives are approximated by the mesh-free least squares-based finite difference (LSFD) scheme using the functional values at centers of current cell and its neighboring cells. In the time-dependent term, the volume integral of solution function over the control cell results in a pre-multiplied coefficient matrix. This matrix connects the functional values at cell centers of the current cell and its neighboring cells. As a consequence, the resultant equation system is implicit in nature. In the work of Ref. 27, the point iterative method is applied to solve the equation system due to its easy implementation and modest memory requirement. The corresponding results show that, in comparison with k -exact method, the high-order LSFD-FV method is slightly more accurate and efficient. However, the point iterative method also suffers from low computational efficiency. In addition, the implicit nature of the LSFD-FV method has not been fully considered when the point iterative method is applied. Therefore, for practical applications, it is desirable to develop a more efficient LSFD-FV method which takes full advantage of its implicit nature.

The implicit time-stepping methods are well developed and they have been applied in high-order methods to solve various flow problems. For steady problems, the implicit lower-upper symmetric Gauss–Seidel (LU-SGS) scheme^{28–30} has drawn amounts of attention due to its simplicity and fast convergence. Even for unsteady problems, the LU-SGS scheme is also widely used to efficiently march the solution in the pseudo time constructed by the dual time stepping (DTS)³¹ method. For example, the DTS method coupled with the LU-SGS scheme was applied in the high-order compact CPR method developed by Cox *et al.*³² In their work, the LU-SGS scheme with backward Euler discretization was used to compute the solution in pseudo time, while a second-order backward difference formulation (BDF2) was used to march in physical time. However, BDF2 only has the second-order of accuracy so the physical time step has to be chosen as a small constant to ensure that the total accuracy does not degrade due to the large errors resulting from the temporal discretization. Thus, even though LU-SGS offers the high computational efficiency in the pseudo time step, the whole unsteady computation process is still time-consuming. In order to match the temporal accuracy with the spatial accuracy, high-order implicit time integration algorithms become fashionable. One representative scheme is the explicit first stage, singly diagonally implicit Runge–Kutta (ESDIRK) method,³³ which has various applications^{34,35} with its temporal accuracy well validated. Moreover, it is proven that the ESDIRK method is more efficient than the explicit Runge–Kutta method. Thus, in this study, the ESDIRK method and the LU-SGS method are applied in the LSFD-FV method on unstructured grids for solving two-dimensional incompressible

flow problems. The efficiency and convergence behavior of the current implicit least squares-based finite difference-finite volume (ILSFD-FV) method are investigated in detail. As shown in this paper, a significant speed-up relative to the explicit LSFD-FV method is demonstrated.

II. HIGH-ORDER IMPLICIT LEAST SQUARE-BASED FINITE DIFFERENCE-FINITE VOLUME (ILSFD-FV) METHOD

A. Governing equations and spatial discretization for high-order LSFD-FV method

In this work, the lattice Boltzmann flux solver (LBFS)^{38,39} will be applied to simultaneously evaluate the viscous and inviscid fluxes of the weakly compressible Navier–Stokes (N–S) equations. Specifically, through the Chapman–Enskog expansion analysis, the weakly compressible N–S equations can be derived from the lattice Boltzmann equation (LBE) in continuum flow regime.^{40–42} When the density variation is small and the Mach number (Ma) is low ($Ma < 0.3$), incompressible flows can be well simulated. For two-dimensional simulation, the recovered governing equations based on mass and momentum conservation laws in the low Mach number limit are

$$\frac{\partial \rho}{\partial t} + \nabla \cdot (\rho \mathbf{u}) = 0, \tag{1}$$

$$\frac{\partial \rho \mathbf{u}}{\partial t} + \nabla \cdot (\rho \mathbf{u} \mathbf{u} + p \mathbf{I}) = \nu \nabla \cdot [\nabla \rho \mathbf{u} + (\nabla \rho \mathbf{u})^T], \tag{2}$$

where ρ is the density, $\mathbf{u} = (u, v)$ is the velocity vector, and p and ν are, respectively, the pressure and kinematic viscosity of the fluid flow. In this weakly compressible model, the pressure is calculated by the equation of state, i.e., $p = \rho c_s^2$, where c_s denotes the sound speed which has the value of $c_s = 1/\sqrt{3}$ for the nine-velocity model.^{38,43,44} The kinematic viscosity of fluid is related to the relaxation parameter τ via $\nu = (\tau - 0.5)c_s^2 \delta t$ through Chapman–Enskog expansion analysis.^{38,39} δt is the streaming distance which is solely used during the local reconstruction of the LBE solution at the cell interface. The details of these parameters can refer to the references.^{27,38–42} \mathbf{I} is the unit tensor. Equations (1) and (2) can be written in a conservative form as

$$\frac{\partial \mathbf{W}}{\partial t} + \nabla \cdot \mathbf{F} = 0, \tag{3}$$

where the vector of conservative variables \mathbf{W} and the vector of fluxes \mathbf{F} are given by

$$\mathbf{W} = \begin{bmatrix} \rho \\ \rho \mathbf{u} \end{bmatrix}, \quad \mathbf{F} = \begin{bmatrix} F_\rho \\ F_{\rho \mathbf{u}} \end{bmatrix}. \tag{4}$$

By incorporating the divergence theorem and Gaussian quadrature, the integral form of Eq. (3) over a control cell Ω_i can be semi-discretized as

$$\frac{d}{dt} \left(\int_{\Omega_i} \mathbf{W} d\Omega \right) = - \sum_{edge=1}^{n_{edge}} \sum_{GQp=1}^{n_{GQp}} (\mathbf{F}_{edge,GQp} \cdot \mathbf{n}_{edge}) A_{edge} w_{GQp}, \tag{5}$$

where $\mathbf{n}_{edge} = (n_x, n_y)$ represents the unit normal vector of the cell interface in the global Cartesian coordinate system, n_{GQp} denotes the number of Gaussian quadrature points on each edge, n_{edge} is the number of cell edges of the cell Ω_i , A is the interface area, and w_{GQp} denotes a quadrature weight.

In the high-order LSFDFV method,²⁷ in order to get higher-order numerical solutions of flow variables within the control cell, a high-order polynomial which is also used to interpolate functional value at the quadrature points along the cell interface for evaluation of numerical fluxes is applied. For the cubic approximation in the 2D case, this high-order polynomial can be given by applying the Taylor series expansion to the flow variable at the reference point i , i.e., the cell center of the control cell Ω_i , as

$$\begin{aligned}
 W(x, y) = & W_i + \frac{\partial W}{\partial x} \Big|_i (x - x_i) + \frac{\partial W}{\partial y} \Big|_i (y - y_i) \\
 & + \frac{\partial^2 W}{\partial x^2} \Big|_i \frac{(x - x_i)^2}{2} + \frac{\partial^2 W}{\partial y^2} \Big|_i \frac{(y - y_i)^2}{2} \\
 & + \frac{\partial^2 W}{\partial x \partial y} \Big|_i (x - x_i)(y - y_i) + \frac{\partial^3 W}{\partial x^3} \Big|_i \frac{(x - x_i)^3}{6} \\
 & + \frac{\partial^3 W}{\partial y^3} \Big|_i \frac{(y - y_i)^3}{6} + \frac{\partial^3 W}{\partial x^2 \partial y} \Big|_i \frac{(x - x_i)^2 (y - y_i)}{2} \\
 & + \frac{\partial^3 W}{\partial y^2 \partial x} \Big|_i \frac{(y - y_i)^2 (x - x_i)}{2}.
 \end{aligned} \tag{6}$$

Equation (6) indicates that the functional value of arbitrary points inside the control cell Ω_i can be approximated with the fourth-order of accuracy. When Eq. (6) is substituted into Eq. (5), it involves 10 unknowns at the cell center (1—functional value, 2—first-order derivatives, 3—second-order derivatives, and 4—third-order derivatives). In fact, integrating Eq. (6) over the control cell Ω_i gives the following equation:

$$\int_{\Omega_i} W(x, y) d\Omega = \Omega_i W_i + dW_i^T C_i, \tag{7}$$

with

$$\begin{aligned}
 dW_i^T = & \left[\frac{\partial W}{\partial x} \Big|_i, \frac{\partial W}{\partial y} \Big|_i, \frac{\partial^2 W}{\partial x^2} \Big|_i, \frac{\partial^2 W}{\partial y^2} \Big|_i, \frac{\partial^2 W}{\partial x \partial y} \Big|_i, \right. \\
 & \left. \frac{\partial^3 W}{\partial x^3} \Big|_i, \frac{\partial^3 W}{\partial y^3} \Big|_i, \frac{\partial^3 W}{\partial x^2 \partial y} \Big|_i, \frac{\partial^3 W}{\partial y^2 \partial x} \Big|_i \right], \\
 C_i^T = & \left[\overline{x^1 y^0}_i, \overline{x^0 y^1}_i, \frac{\overline{x^2 y^0}_i}{2}, \frac{\overline{x^0 y^2}_i}{2}, \overline{x^1 y^1}_i, \frac{\overline{x^3 y^0}_i}{6}, \right. \\
 & \left. \frac{\overline{x^0 y^3}_i}{6}, \frac{\overline{x^2 y^1}_i}{2}, \frac{\overline{x^1 y^2}_i}{2} \right],
 \end{aligned} \tag{8}$$

where $\overline{x^n y^m}_i = \int_{\Omega_i} (x - x_i)^n (y - y_i)^m d\Omega$. Equation (7) has 10 unknowns but Eq. (5) only provides one equation for each cell. Obviously, the problem is not well-posed. As indicated in the LSFDFV method,²⁷ the unknown derivatives in Eq. (7) can be approximated by the meshless LSFDFV method,^{36,37} which is also based on the two-dimensional Taylor series expansion as shown in Eq. (6). By applying Eq. (6) to 9 neighboring cells of Ω_i , the following linear equation system with 9 derivatives as unknowns can be obtained:

$$S_i dW_i = \Delta W_i, \tag{9}$$

where the matrix S and ΔW are

$$\begin{aligned}
 S_i = & \begin{pmatrix} \Delta x_{i1} & \Delta y_{i1} & \frac{\Delta x_{i1}^2}{2} & \frac{\Delta y_{i1}^2}{2} & \Delta x_{i1} \Delta y_{i1} & \frac{\Delta x_{i1}^3}{6} & \frac{\Delta y_{i1}^3}{6} & \frac{\Delta x_{i1}^2 \Delta y_{i1}}{2} & \frac{\Delta y_{i1}^2 \Delta x_{i1}}{2} \\ \Delta x_{i2} & \Delta y_{i2} & \frac{\Delta x_{i2}^2}{2} & \frac{\Delta y_{i2}^2}{2} & \Delta x_{i2} \Delta y_{i2} & \frac{\Delta x_{i2}^3}{6} & \frac{\Delta y_{i2}^3}{6} & \frac{\Delta x_{i2}^2 \Delta y_{i2}}{2} & \frac{\Delta y_{i2}^2 \Delta x_{i2}}{2} \\ \vdots & \vdots \\ \Delta x_{i9} & \Delta y_{i9} & \frac{\Delta x_{i9}^2}{2} & \frac{\Delta y_{i9}^2}{2} & \Delta x_{i9} \Delta y_{i9} & \frac{\Delta x_{i9}^3}{6} & \frac{\Delta y_{i9}^3}{6} & \frac{\Delta x_{i9}^2 \Delta y_{i9}}{2} & \frac{\Delta y_{i9}^2 \Delta x_{i9}}{2} \end{pmatrix}, \\
 \Delta x_{ij} = & x_j - x_i, \quad \Delta y_{ij} = y_j - y_i, \quad j = 1, \dots, 9, \\
 \Delta W_i^T = & [W_{i1} - W_i, W_{i2} - W_i, \dots, W_{ij} - W_i],
 \end{aligned} \tag{10}$$

where W_{ij} is the functional value at the center of the j th neighboring cell to the current cell i . By solving equation system (9), the expression of the derivative vector dW can be obtained in terms of ΔW . However, due to unstructured cell distribution for a general case, the equation system may be ill-conditioned or even singular. To overcome this difficulty, the local scaling technique and least squares optimization were introduced, where Eq. (6) is applied at more than 9 neighboring points. The details of these techniques can be referred to the work of Ding *et al.*³⁶ Following the derivations in the work of Liu *et al.*,²⁷ the unknown derivatives can be computed by

$$dW = [\bar{D}(\bar{S}^T W_e \bar{S})^{-1} \bar{S}^T W_e] \Delta W = K \Delta W, \tag{11}$$

where

$$\begin{aligned}
 \bar{S}^T = & [s_1, s_2, \dots, s_N], \quad N > 9 \\
 s_j = & \left[\Delta \bar{x}_j, \Delta \bar{y}_j, \frac{\Delta \bar{x}_j^2}{2}, \frac{\Delta \bar{y}_j^2}{2}, \Delta \bar{x}_j \Delta \bar{y}_j, \frac{\Delta \bar{x}_j^3}{6}, \frac{\Delta \bar{y}_j^3}{6}, \frac{\Delta \bar{x}_j^2 \Delta \bar{y}_j}{2}, \frac{\Delta \bar{y}_j^2 \Delta \bar{x}_j}{2} \right], \\
 & j = 1, \dots, N.
 \end{aligned} \tag{12}$$

In Eqs. (11) and (12), the distance relations are $(\Delta \bar{x}, \Delta \bar{y}) = (\Delta x/d_0, \Delta y/d_0)$, locally scaled by the radius d_0 which is the farthest Euclidean distance from the reference point i . The scaling matrix \bar{D} only contains diagonal elements of the inverse scaling. W_e is

the $N \times N$ diagonal matrix formed by applying the weighting function at N supporting points. The weighting coefficient matrix K is related to the grid uniquely. When static grids are used, the mesh point distribution does not change. Therefore, K is computed for only one time and then stored for the following calculations, which can save the computational effort.

Once the derivatives are approximated by the LSFDF method, Eq. (6) can be used to interpolate the functional values at corresponding locations. Then, following the process in the LSFDF-FV method,²⁷ the numerical fluxes at the cell interface can be evaluated by LBFS^{38,39} which evaluates the inviscid and viscous fluxes simultaneously. Moreover, after substituting Eq. (7) into Eq. (5), the resultant ordinary differential equations are solved to update the conservative variables at the cell center by implicit time marching techniques. The details will be discussed in Sec. II B.

B. Implicit time integration scheme for high-order LSFDF-FV method

As shown in Eq. (7), when Taylor series expansion form (6) is substituted into the volume integral of solution function over the control cell i , we have

$$\int_{\Omega_i} W(x, y) d\Omega = \Omega_i W_i + dW_i^T C_i = \Omega_i W_i + \sum_{k=1}^9 C_k^i dW_k^i. \quad (13)$$

Equation (13) involves functional value W_i and its spatial derivatives. As shown in Eq. (11), the spatial derivatives can be approximated by the LSFDF scheme in terms of differences between the functional values at the centers of current cell i and its neighboring cells. Thus, we have

$$\begin{aligned} \int_{\Omega_i} W(x, y) d\Omega &= \Omega_i W_i + \sum_{k=1}^9 C_k^i \sum_{j=1}^N K_{k,j}^i \Delta W_{ij} \\ &= \Omega_i W_i + \sum_{k=1}^9 C_k^i \sum_{j=1}^N K_{k,j}^i (W_{ij} - W_i) \\ &= \left(\Omega_i - \sum_{k=1}^9 C_k^i \sum_{j=1}^N K_{k,j}^i \right) W_i + \sum_{j=1}^N \left(\sum_{k=1}^9 C_k^i K_{k,j}^i \right) W_{ij} \\ &= M_{i,i} W_i + \sum_{j=1}^N M_{i,j} W_{ij}. \end{aligned} \quad (14)$$

As a result, the following matrix form can be obtained from Eq. (5) when Eq. (14) is applied to all control cells,

$$M \frac{\partial W}{\partial t} = -R(W), \quad (15)$$

where W and R are, respectively, the solution vector and the vector of flux contribution for all control cells, and M is a sparse matrix formed by coefficients on the right hand side of Eq. (14). Apparently, the appearance of the matrix M endows the high-order LSFDF-FV method with the implicit nature.

In order to update the solution, the equation system (15) has to be solved. When a steady state problem is considered, the time accuracy is of no importance and the widely used implicit LU-SGS²⁸⁻³⁰ method can be applied to improve the efficiency of this high-order

LSFDF-FV method. In the implementation of the implicit LU-SGS method, Eq. (15) should be rewritten as

$$M \frac{W^{n+1} - W^n}{\Delta t} = -R^{n+1}(W), \quad (16)$$

where Δt denotes the time step which is determined by the Courant-Friedrichs-Lewy (CFL) condition. The superscript “ n ” and “ $n + 1$ ” represent the current time level at time t and the new time level at time $t + \Delta t$, respectively. Then, the residual R^{n+1} is linearized about the current time level n as

$$R^{n+1} \approx R^n + \left(\frac{\partial R}{\partial W} \right)^n \Delta W^n, \quad (17)$$

where $\Delta W^n = W^{n+1} - W^n$ and $\partial R / \partial W$ is the flux Jacobian. After substituting Eq. (17) into Eq. (16), the following equation is obtained:

$$\left[\frac{M}{\Delta t} + \left(\frac{\partial R}{\partial W} \right)^n \right] \Delta W^n = -R^n(W). \quad (18)$$

The term in the square bracket on the left-hand side of Eq. (18) is referred to as the implicit operator. Apparently, this implicit operator contains two parts which are the coefficient matrix M and the flux Jacobian $\partial R / \partial W$. These two parts constitute a large, sparse, and non-symmetric system matrix with dimensions equal to the total number of cells. Thus, the implicit nature of the high-order LSFDF-FV method is combined into the implicit operator naturally and conveniently and they can be treated together. Generally, the direct matrix inversion for this term is expensive in terms of the computational effort and the virtual memory. To solve Eq. (18), in the LU-SGS framework, the implicit operator is factorized into the diagonal and off diagonal terms, i.e.,

$$\left[\frac{M}{\Delta t} + \left(\frac{\partial R}{\partial W} \right)^n \right] \Delta W^n = (D + L)D^{-1}(D + U)\Delta W^n, \quad (19)$$

where L , U , and D are the matrices of strictly lower triangular, upper triangular, and diagonal terms, respectively. Equation (18) is then replaced by the following equation:

$$(D + L)D^{-1}(D + U)\Delta W^n = -R^n(W). \quad (20)$$

In practical implementation, the system matrix of implicit operator in Eq. (18) can be simplified. For the term of the coefficient matrix M , as indicated in our previous work,²⁷ it can be replaced by the identity matrix or the diagonal matrix which shares the diagonal elements with the coefficient matrix M . In addition, since steady state solutions are the only concerns and in order to reduce the numerical complexity, the flux Jacobian matrix $\partial R / \partial W$ is not evaluated analytically but approximated by a simplified formulation. For illustrative purpose, on unstructured grids, we take the control cell Ω_i as the reference cell and Ω_j represents its neighboring cells. Hence, the flux Jacobian is approximately evaluated by the flux splitting method with the spectral radius via

$$\begin{aligned} \frac{\partial R_i}{\partial W} \Delta W = \sum_{j \in C(i)} \frac{\partial R_i}{\partial W_j} \Delta W_j = \sum_{j \in N(i)} \frac{1}{2} \left[(\Delta F_{c,i} + \Delta F_{c,j}) \cdot n_{ij} \right. \\ \left. + (\Lambda_{ij} + \hat{\Lambda}_{ij}) (\Delta W_i - \Delta W_j) \right] A_{ij}, \end{aligned} \quad (21)$$

where $C(i)$ is the set of cell i and its neighbor cells and $N(i)$ is the set of neighbor cells of cell i . F_c is the convective flux and

$\Delta F_{c,j} = F_c(W_j + \Delta W_j) - F_c(W_j)$. $\Lambda_{ij} = |\mathbf{V}_{ij} \cdot \mathbf{n}_{ij}| + c_{sij}$ represents the maximal eigenvalue of the convective flux Jacobian. Here, the subscript ij denotes the face which is shared by control cell i and j . \mathbf{V} and c_s denote the velocity vector and the sound speed, respectively. The factor $\hat{\Lambda}_{ij} = \frac{1}{r_{ij}} [\max(\frac{4}{3\rho_{ij}}, \frac{\gamma}{\rho_{ij}} \frac{\mu_{ij}}{Pr})]$ reflects the maximum viscous eigenvalue, where γ is the ratio of specific heat coefficient, Pr denotes the Prandtl number, μ represents the dynamic viscosity, and r_{ij} is the distance between the barycenter of cells i and j .

With the simplifications for the coefficient matrix M and the flux Jacobian $\partial R/\partial W$, the operators L , U , and D for unstructured grids can be given as

$$\begin{aligned} L &= \sum_{j \in L(i)} \frac{1}{2} \left[\frac{\Delta F_{c,j}}{\Delta W_j} \cdot \mathbf{n}_{ij} - (\Lambda_{ij} + \hat{\Lambda}_{ij}) \mathbf{I} \right] A_{ij}, \\ U &= \sum_{j \in U(i)} \frac{1}{2} \left[\frac{\Delta F_{c,j}}{\Delta W_j} \cdot \mathbf{n}_{ij} - (\Lambda_{ij} + \hat{\Lambda}_{ij}) \mathbf{I} \right] A_{ij}, \\ D &= \left[\frac{M_{i,i}}{\Delta t} + \frac{1}{2} \sum_{j \in N(i)} (\Lambda_{ij} + \hat{\Lambda}_{ij}) A_{ij} \right] \mathbf{I}, \end{aligned} \tag{22}$$

where $L(i)$ and $U(i)$ denote the nearest neighbors of cell i which belong to the lower and upper matrices, respectively. Finally, Eq. (20) can be solved by the following forward and backward sweep procedures for the reference cell Ω_i :

$$\begin{aligned} \Delta W_i^* &= D^{-1} \left\{ -\mathbf{R}_i^n - \sum_{j \in L(i)} \frac{1}{2} \left[\Delta F_{c,j}^* \cdot \mathbf{n}_{ij} - (\Lambda_{ij} + \hat{\Lambda}_{ij}) \mathbf{I} \Delta W_j^* \right] A_{ij} \right\}, \\ \Delta W_i^n &= \Delta W_i^* - D^{-1} \left\{ \sum_{j \in U(i)} \frac{1}{2} \left[\Delta F_{c,j}^n \cdot \mathbf{n}_{ij} - (\Lambda_{ij} + \hat{\Lambda}_{ij}) \mathbf{I} \Delta W_j^n \right] A_{ij} \right\}, \end{aligned} \tag{23}$$

with

$$\begin{aligned} \Delta F_{c,j}^* &= F_c(W_j^n + \Delta W_j^*) - F_c(W_j^n), \\ \Delta F_{c,j}^n &= F_c(W_j^n + \Delta W_j^n) - F_c(W_j^n), \end{aligned} \tag{24}$$

where ΔW^* is the intermediate solution in the forward sweep. Once the solution correction ΔW^n is obtained, the macroscopic flow variables can be updated by $W^{n+1} = \Delta W^n + W^n$.

For unsteady flow simulation, the temporal accuracy is also of great importance. In order to reflect the implicit characteristic of this LSFD-FV method and improve its efficiency, the third-order

four-stage ESDIRK method with DTS approach is applied to simulate the unsteady flow problems. The details of the ESDIRK method are as follows:

$$W^k = W^n - \Delta t \sum_{j=1}^k a_{kj} M^{-1} R(W^j), \quad k = 1, 2, \dots, \alpha, \tag{25}$$

$$W^{n+1} = W^n - \Delta t \sum_{j=1}^{\alpha} b_j M^{-1} R(W^j), \tag{26}$$

where α is the number of stages, a_{kj} are the stage weights (cf. Table I), and b_j are the weights. The vectors W^k , W^n , and W^{n+1} are the solutions at stage k , the previous time level n , and the next time level $n+1$, respectively. Note that, for this ESDIRK scheme used in our case, the last stage gives the solution at the new time level, i.e., $W^{n+1} = W^\alpha$. Therefore, it is unnecessary to carry out computation through Eq. (26). However, the residuals of every stage have to be stored. In order to advance W^k from the time level n to $n+1$, we have to solve the sequential set of $\alpha - 1$ nonlinear algebraic equations defined in Eq. (25). By applying such an α -stage ESDIRK method, at each stage k , Eq. (15) can be discretized as

$$M \frac{W^k - W^n}{\Delta t} = -a_{kk} R(W^k) - \sum_{j=1}^{k-1} a_{kj} R(W^j), \quad k = 1, \dots, \alpha. \tag{27}$$

Generally, it is difficult to solve Eq. (27) in its present form. To solve this problem, the DTS approach is used. The pseudo time term $\partial W^k/\partial \tau$ is added to Eq. (27), yielding the expression

$$M \frac{dW^k}{d\tau} + M \frac{W^k - W^n}{\Delta t} = -a_{kk} R(W^k) - \sum_{j=1}^{k-1} a_{kj} R(W^j). \tag{28}$$

Then the time integration scheme for one pseudo time step is

$$\begin{aligned} M \frac{W^{k,s+1} - W^{k,s}}{\Delta \tau} &= -M \frac{W^{k,s+1} - W^n}{\Delta t} - a_{kk} R(W^{k,s+1}) - \sum_{j=1}^{k-1} a_{kj} R(W^j) \\ &= -R^*(W^{k,s+1}), \end{aligned} \tag{29}$$

where $\Delta \tau$ is the pseudo time step, s is the step of the pseudo time, and $R^*(W^{k,s+1})$ is the unsteady residual. Note that the subscript “ i ” has been removed for simplicity in Eqs. (28) and (29). In this way, the solution at each stage of ESDIRK method can be obtained by treating Eq. (29) as a steady-state problem, where the matrix M on the left side

TABLE I. Butcher tableau for ESDIRK scheme.

a_{1j}	0	0	0	0
a_{2j}	1 767 732 205 903	1 767 732 205 903	0	0
	4 055 673 282 236	4 055 673 282 236		
a_{3j}	2 746 238 789 719	-640 167 445 237	1 767 732 205 903	0
	10 658 868 560 708	6 845 629 431 997	4 055 673 282 236	
a_{4j}	1 471 266 399 579	-4 482 444 167 858	11 266 239 266 428	1 767 732 205 903
	7 840 856 788 654	7 529 755 066 697	11 593 286 722 821	4 055 673 282 236
b_j	a_{41}	a_{42}	a_{43}	a_{44}

can be simplified by the diagonal matrix without affecting the accuracy.

To discretize the pseudo-time derivative with an implicit solver, the unsteady residual $\mathbf{R}^*(\mathbf{W}^{k,s+1})$ given in Eq. (29) is linearized with respect to the known pseudo-time level s at stage k as

$$\begin{aligned} \mathbf{R}^*(\mathbf{W}^{k,s+1}) &\approx \mathbf{R}^*(\mathbf{W}^{k,s}) + \left(\frac{\partial \mathbf{R}^*}{\partial \mathbf{W}}\right)^{k,s} \Delta \mathbf{W}^{k,s} \\ &= \mathbf{R}^*(\mathbf{W}^{k,s}) + \left[\frac{\mathbf{M}}{\Delta t} + a_{kk} \left(\frac{\partial \mathbf{R}}{\partial \mathbf{W}}\right)^{k,s}\right] \Delta \mathbf{W}^{k,s}, \end{aligned} \quad (30)$$

where $\Delta \mathbf{W}^{k,s} = \mathbf{W}^{k,s+1} - \mathbf{W}^{k,s}$. By substituting Eq. (30) into Eq. (29), the implicit integration in the pseudo time with the ESDIRK method is obtained in a non-factorized form as

$$\left[\frac{\mathbf{M}}{\Delta \tau} + \frac{\mathbf{M}}{\Delta t} + a_{kk} \left(\frac{\partial \mathbf{R}}{\partial \mathbf{W}}\right)^{k,s}\right] \Delta \mathbf{W}^{k,s} = -\mathbf{R}^*(\mathbf{W}^{k,s}), \quad k = 1, \dots, \alpha, \quad (31)$$

where

$$\mathbf{R}^*(\mathbf{W}^{k,s}) = \mathbf{M} \frac{\mathbf{W}^{k,s}}{\Delta t} + a_{kk} \mathbf{R}(\mathbf{W}^{k,s}) + \left[-\mathbf{M} \frac{\mathbf{W}^n}{\Delta t} + \sum_{j=1}^{k-1} a_{kj} \mathbf{R}(\mathbf{W}^j)\right]. \quad (32)$$

It is noteworthy that the matrix \mathbf{M} in $\mathbf{R}^*(\mathbf{W}^{k,s})$ cannot be simplified to preserve the accuracy while \mathbf{M} in the implicit operator on the left-hand side of Eq. (31) can be simplified to combine with the LU-SGS method. Based on the factorization of the implicit operator in Eq. (31) and the simplifications stated above, at the k th stage of the ESDIRK method, the operators \mathbf{L} , \mathbf{U} , and \mathbf{D} read

$$\begin{aligned} \mathbf{L} &= \sum_{j \in L(i)} \frac{1}{2} \left[\frac{\Delta F_{c,j}}{\Delta W_j} \cdot \mathbf{n}_{ij} - (\Lambda_{ij} + \hat{\Lambda}_{ij}) \mathbf{I} \right] A_{ij}, \\ \mathbf{U} &= \sum_{j \in U(i)} \frac{1}{2} \left[\frac{\Delta F_{c,j}}{\Delta W_j} \cdot \mathbf{n}_{ij} - (\Lambda_{ij} + \hat{\Lambda}_{ij}) \mathbf{I} \right] A_{ij}, \\ \mathbf{D} &= \left[\frac{M_{i,i}}{\Delta \tau} + \frac{M_{i,i}}{\Delta t} + \frac{a_{kk}}{2} \sum_{j \in N(i)} (\Lambda_{ij} + \hat{\Lambda}_{ij}) A_{ij} \right] \mathbf{I}. \end{aligned} \quad (33)$$

Then, the following two-step inversion procedure is obtained, i.e.,

$$\begin{aligned} \Delta \mathbf{W}_i^{(1)} &= \mathbf{D}^{-1} \left\{ -\mathbf{R}^*(\mathbf{W}_i^s) - \sum_{j \in L(i)} \frac{1}{2} \left[\frac{\Delta F_{c,j}^{(1)}}{\Delta W_j} \cdot \mathbf{n}_{ij} - (\Lambda_{ij} + \hat{\Lambda}_{ij}) \mathbf{I} \right] \Delta \mathbf{W}_j^{(1)} \right\} A_{ij}, \\ \Delta \mathbf{W}_i^s &= \Delta \mathbf{W}_i^{(1)} - \mathbf{D}^{-1} \left\{ \sum_{j \in U(i)} \frac{1}{2} \left[\frac{\Delta F_{c,j}^s}{\Delta W_j} \cdot \mathbf{n}_{ij} - (\Lambda_{ij} + \hat{\Lambda}_{ij}) \mathbf{I} \right] \Delta \mathbf{W}_j^s \right\} A_{ij}, \end{aligned} \quad (34)$$

with

$$\begin{aligned} \Delta \mathbf{F}_{c,j}^{(1)} &= \mathbf{F}_c(\mathbf{W}_j^s + \Delta \mathbf{W}_j^{(1)}) - \mathbf{F}_c(\mathbf{W}_j^s), \\ \Delta \mathbf{F}_{c,j}^s &= \mathbf{F}_c(\mathbf{W}_j^s + \Delta \mathbf{W}_j^s) - \mathbf{F}_c(\mathbf{W}_j^s), \end{aligned} \quad (35)$$

where $\Delta \mathbf{W}^{(1)}$ is the intermediate solution correction. Note that the subscript “ k ” has been omitted for simplicity in Eqs. (33)–(35). Once

\mathbf{W}^s at the stage k meets the convergence tolerance of the pseudo steady state solution, \mathbf{W}^s will be set as the original value for the computation at the next stage $k + 1$.

III. NUMERICAL EXAMPLES

In this section, the performance of the developed high-order ILSFD-FV method is validated by both steady and unsteady incompressible flow problems on arbitrary grids. In the simulation, for solving Eq. (15), both implicit method and explicit method are applied in order to assess the speedup ratio. Specifically, for steady flow problems, the matrix-free LU-SGS scheme is adopted as the implicit method while the explicit method refers to the Euler explicit scheme. For calculating the unsteady flow problems, the implicit ESDIRK time integration scheme introduced above and the total variation diminishing-Runge-Kutta (TVD-RK)¹² scheme are used as the implicit method and the explicit method, respectively. Unless otherwise stated, the CFL number for steady computations by the implicit LU-SGS method is taken as 100. For the unsteady flow problem, the physical time step is determined based on different flow problems and not restricted by the CFL condition. Basically, the physical time step is set as one value corresponding to a maximal CFL number of about 150. In each physical time step, the CFL number for the local pseudo-time iterations is taken as 5 for stability and these inner iterations are performed until convergence is achieved. The convergence criterion for the inner iteration is a drop of five orders of magnitude of the unsteady residual for the velocity field. All simulations are done on a personal computer (PC) with 2.30 GHz central processing unit (CPU).

A. Decaying vortex flow on unstructured mesh

First, the decaying vortex flow problem^{45,46} is solved to conduct the convergence study for the developed ILSFD-FV method. For reference purpose, the explicit TVD-RK method is also performed to compare with the implicit counterpart. The analytical solution of this problem satisfying the 2D unsteady incompressible N–S equation reads

$$\begin{aligned} u(x, y, t) &= -U \cos(\pi x/L) \sin(\pi y/L) e^{-2\pi^2 U t / (ReL)}, \\ v(x, y, t) &= U \sin(\pi x/L) \cos(\pi y/L) e^{-2\pi^2 U t / (ReL)}, \\ \rho(x, y, t) &= \rho_0 - \frac{\rho_0 U^2}{4c_s^2} [\cos(2\pi x/L) + \cos(2\pi y/L)] e^{-4\pi^2 U t / (ReL)}, \end{aligned} \quad (36)$$

where U and ρ_0 are the initial velocity amplitude and the reference density. The relaxation parameter τ is chosen as 0.8, and ρ_0 is set as 1. The computation is conducted on a square domain $[-L, L] \times [-L, L]$ at $Re = UL/\nu = 10$. Periodic boundary condition is imposed on all boundaries. Solutions at the non-dimensional time $t = L/U = 1$ are extracted to compute the relative error of velocity component u using the L_2 norm and L_1 norm which are defined as

$$\begin{aligned} L_1(u) &= \frac{1}{N_{cell}} \sum_{i=1}^{N_{cell}} \left(\left| \frac{u_i - u_i^e}{U} \right| \right), \\ L_2(u) &= \left(\frac{1}{N_{cell}} \sum_{i=1}^{N_{cell}} \left(\frac{u_i - u_i^e}{U} \right)^2 \right)^{\frac{1}{2}}, \end{aligned} \quad (37)$$

where u_i and u_i^e refer to the numerical result and the analytical solution, respectively. N_{cell} denotes the number of the cell.

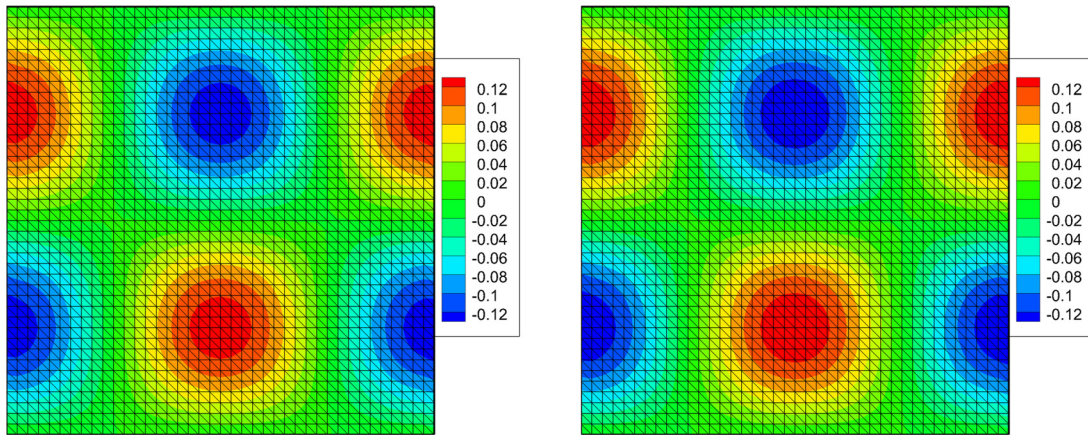


FIG. 1. Velocity contours obtained by the implicit LSFD-FV method (left) and the explicit LSFD-FV method (right) on the regular triangular grid where $h = 2/40$ for decaying vortex flow problem at $t = 1$ and $Re = 10$.

TABLE II. Relative errors of velocity component u and accuracy order of different methods for decaying vortex flow on regular triangular grids.

Scheme	Grid size	L_1 errors	Order	L_2 errors	Order
Explicit method	2/20	2.00×10^{-3}		2.24×10^{-3}	
	2/30	4.06×10^{-4}	3.933	4.55×10^{-4}	3.933
	2/40	1.27×10^{-4}	4.028	1.43×10^{-4}	4.032
	2/80	7.34×10^{-6}	4.117	8.23×10^{-6}	4.115
Implicit method	2/20	1.89×10^{-3}		2.12×10^{-3}	
	2/30	3.94×10^{-4}	3.869	4.41×10^{-4}	3.868
	2/40	1.25×10^{-4}	3.990	1.40×10^{-4}	3.991
	2/80	6.93×10^{-6}	4.173	7.81×10^{-6}	4.164

In the computation, four regular triangular grids with the mesh size $h = 2/20, 2/30, 2/40,$ and $2/80$ are used. The physical time step is chosen as a $\Delta t = 0.7h$. The CFL number for the local pseudo time step is 5 and the convergence criterion for pseudo steady state per

physical time step is a drop of five orders of magnitude of the unsteady residual R^* in velocity.

The velocity contours obtained by the ILSFD-FV method and its explicit counterpart on the regular triangular grids of $h = 2/40$ are shown in Fig. 1. L_1 and L_2 norm of errors of the velocity component u and the rates of convergence are tabulated in Table II. The linearly fitted lines of the high-order ILSFD-FV method in Fig. 2 reveal slopes of 4.055 and 4.050 for L_1 and L_2 norm errors, respectively. Such an outcome demonstrates the fourth-order of accuracy of the present ILSFD-FV method for the incompressible flows.

Besides, the effects of the physical time step and the pseudo time step are also investigated in this unsteady case. First, the physical time steps of 0.005, 0.015, 0.03, 0.06, 0.08, and 0.16 are used, respectively. The comparative study is conducted on the mesh with $h = 2/30$ and the CFL number for the local pseudo time step is fixed as 5. Table III compares the corresponding L_1 and L_2 norm of errors of the velocity component u and a very small difference between them can be seen. This observation illustrates that the accuracy of the present scheme is not affected by the physical time step as long as it is within a reasonable range (e.g., $\Delta t \leq t/10$). Then the results of various pseudo time

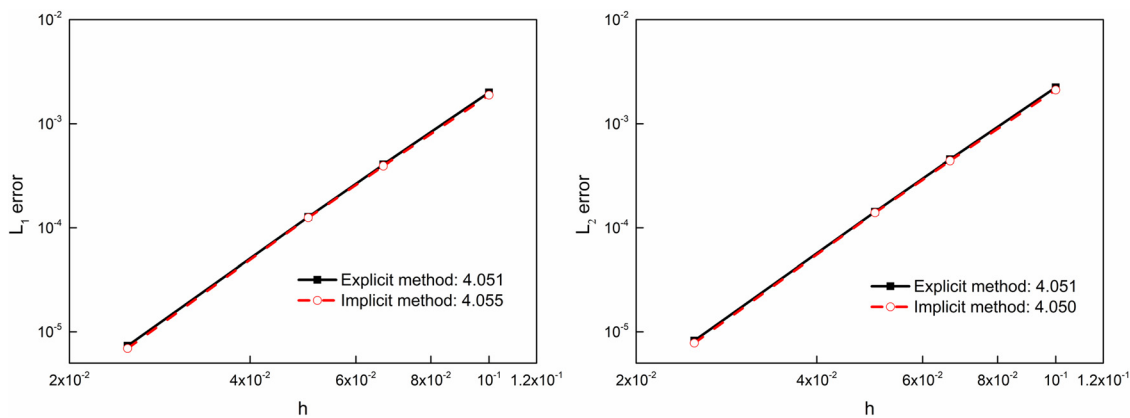


FIG. 2. Convergence studies for 2D decaying vortex flow at $t = 1$. The numbers in the figures denote the slopes of the linearly fitted lines.

TABLE III. Relative errors of velocity component u and accuracy order of different physical time steps for decaying vortex flow on regular triangular grids of the mesh size $h = 2/30$ with the CFL number set as 5 for the pseudo-time iteration.

Physical time size Δt	Maximum inner iteration number	L_1 errors	L_2 errors
0.16	1541	4.83×10^{-4}	4.32×10^{-4}
0.08	822	4.38×10^{-4}	3.91×10^{-4}
0.06	632	4.51×10^{-4}	4.03×10^{-4}
0.03	339	4.48×10^{-4}	4.00×10^{-4}
0.015	198	4.48×10^{-4}	4.00×10^{-4}
0.005	98	4.50×10^{-4}	4.02×10^{-4}

steps that correspond to the CFL numbers of 3, 5, 6, and 7 for inner iterations at each physical time step are quantitatively compared in Table IV. Note that, in this comparison, the mesh with $h = 2/30$ is used and the physical time step is fixed at $\Delta t = 0.05$. From the tabulated errors of the velocity component u , the pseudo time step would not affect the accuracy. However, too large pseudo time step would result in serious stability problem. Meanwhile, the relatively large pseudo time step would lead to a fast convergence rate for the pseudo steady computation at each physical time step.

B. Steady plane Poiseuille flow on uniform mesh

The Poiseuille viscous flow⁴⁷ driven by a uniform pressure gradient is a classic benchmark test for the steady incompressible flow. Its analytical solutions can be easily derived, which provides flexibility to investigate the accuracy of the high-order ILSFD-FV method. From the N-S equations, the analytical solution of the velocity profile for this problem reads

$$u(y) = \frac{(y^2 - hy) \partial p}{2\mu \partial x}, \tag{38}$$

where $\partial p/\partial x$ denotes the pressure gradient. In this simulation, the computational domain is set as $[0, 1] \times [0, 1]$. The height $h = 1$, the dynamic viscosity $\mu = 0.05$ and $\partial p/\partial x = -0.001$, is applied. For comparison purpose, three uniform quadrilateral grids with the size $h = 1/10, 1/20,$ and $1/40$ are used. On the inlet and outlet of the channel, a uniform pressure boundary condition is given. In addition, on the upper and lower solid boundaries, a no-slip boundary condition is enforced.

TABLE IV. Relative errors of velocity component u of different pseudo time steps for decaying vortex flow on regular triangular grids of the mesh size $h = 2/30$ with the physical time step set as $\Delta t = 0.05$.

CFL number	Maximum inner iteration number	CPU time	L_1 errors	L_2 errors
3	1169	427.02	4.410×10^{-4}	3.938×10^{-4}
5	535	200.02	4.411×10^{-4}	3.939×10^{-4}
6	428	151.42	4.410×10^{-4}	3.938×10^{-4}
>7	Diverge	Diverge

Results of the u -component profiles obtained by this high-order ILSFD-FV method on different grids are shown in Fig. 3. Note that all the numerical results match the analytical solution perfectly even using the coarsest grid with $h = 1/10$. These results prove that the ILSFD-FV method can capture the velocity distribution accurately. Furthermore, as the comparison of convergence history in Fig. 4, on the same mesh $h = 1/40$, the implicit method can converge with less iterations and less CPU time used than the explicit one. Additionally, Table V lists the computational effort of the implicit method and the explicit method on three sets of grids. Overall, the iteration steps of the implicit method are less than one-third of the explicit method. Moreover, the speedup ratio of the run time reaches 4.

C. Lid-driven cavity flow on unstructured mesh

The two-dimensional lid-driven flow^{48,49} in a square cavity is one important benchmark case for incompressible viscous flows and this steady case is employed to test the accuracy and efficiency of the present high-order ILSFD-FV method on unstructured grids.

The physical configuration of this case is that the viscous flow in a two-dimensional square cavity is driven by the moving lid with the velocity U_0 to form a circulation flow while other three solid walls keep static with the no-slip boundary condition. In the simulation, the Reynolds number is defined as $Re = U_0 L/\nu$, where L denotes the reference length of the square cavity and $L = 1$. The unstructured grid used is shown in Fig. 5.

First, the constant velocity of the moving lid is set as $U_0 = 0.1$ and the CFL number for the implicit temporal discretization is taken as 1000. Figure 5 shows the computed streamlines at $Re = 1000$ by the high-order ILSFD-FV method. Obviously, the flow structures obtained agree well with the results in the literature.^{38,50} Figure 6 presents the comparisons of the u -velocity and v -velocity profiles along the vertical and horizontal central lines obtained by the present high-order LSFD-FV method coupled with the implicit method and the explicit method,

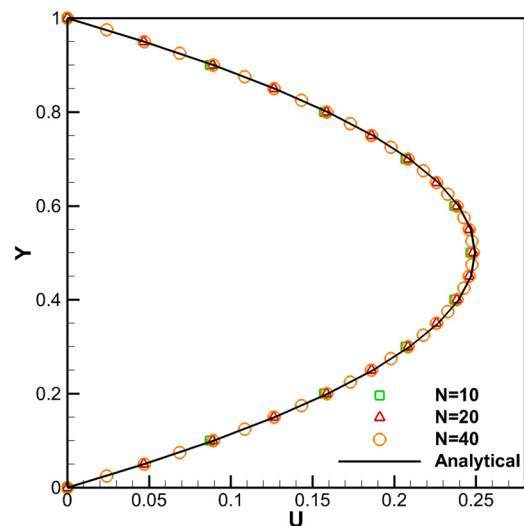


FIG. 3. u -component profiles given by the ILSFD-FV method on the uniform quadrilateral grids. The solid line denotes the analytical solution. Symbols are computed with different mesh points.

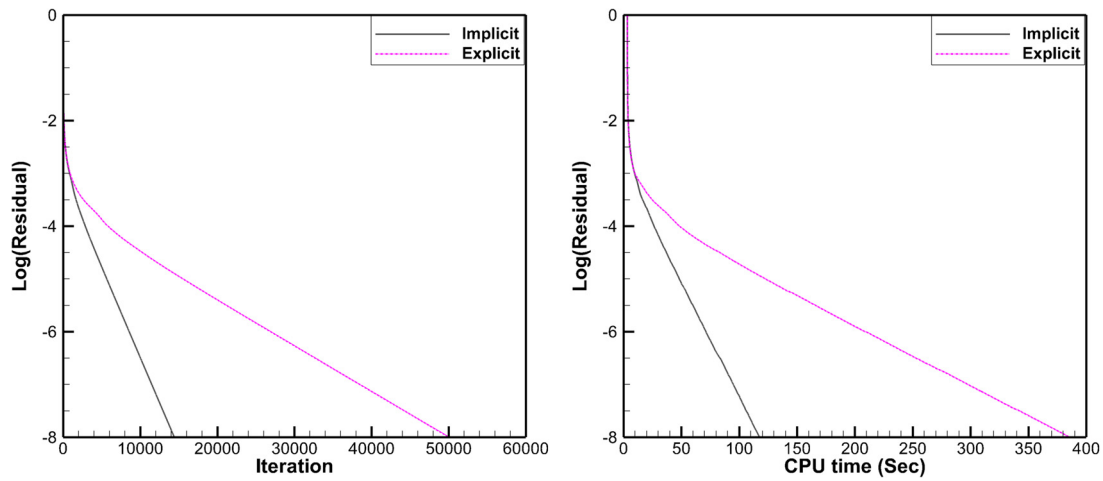


FIG. 4. Comparison of convergence history (left) and CPU time (right) for different temporal discretization methods on uniform quadrilateral grids of $h = 1/40$.

TABLE V. Comparison of the CPU time between the explicit and implicit methods for steady plane Poiseuille flow.

Cells of mesh	Explicit method			Implicit method			Speedup
	Iteration steps	CPU time (s)	L_2 errors	Iteration steps	CPU time (s)	L_2 errors	
100	4265	2.2	3.42×10^{-4}	1163	0.5	3.42×10^{-4}	4.4
400	14 610	26.1	1.96×10^{-4}	4077	7.1	1.96×10^{-4}	3.7
1600	50 083	383.2	1.55×10^{-4}	14 409	114.5	1.54×10^{-4}	3.3

against the benchmark data of Ghia *et al.*⁵¹ at three Reynolds numbers of $Re = 1000, 3200, \text{ and } 5000$. Furthermore, the corresponding convergence history curves are compared in Fig. 7 and Table VI lists the iteration steps and the CPU time used by the implicit method and the

explicit method. From these results, it is clear that the high-order ILSFD-FV method converges at less iteration steps and the corresponding computation time ranges from one-ninth to one-fourteenth of the explicit one.

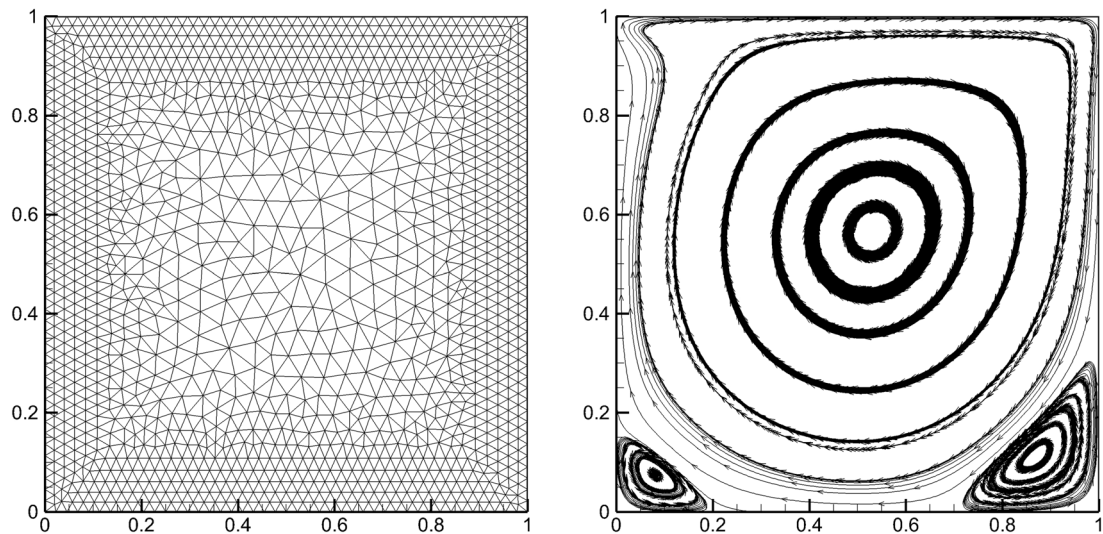


FIG. 5. Lid-driven cavity flow: the unstructured mesh of 2734 cells (left) and streamlines (right) for the high-order ILSFD-FV method at $Re = 1000$.

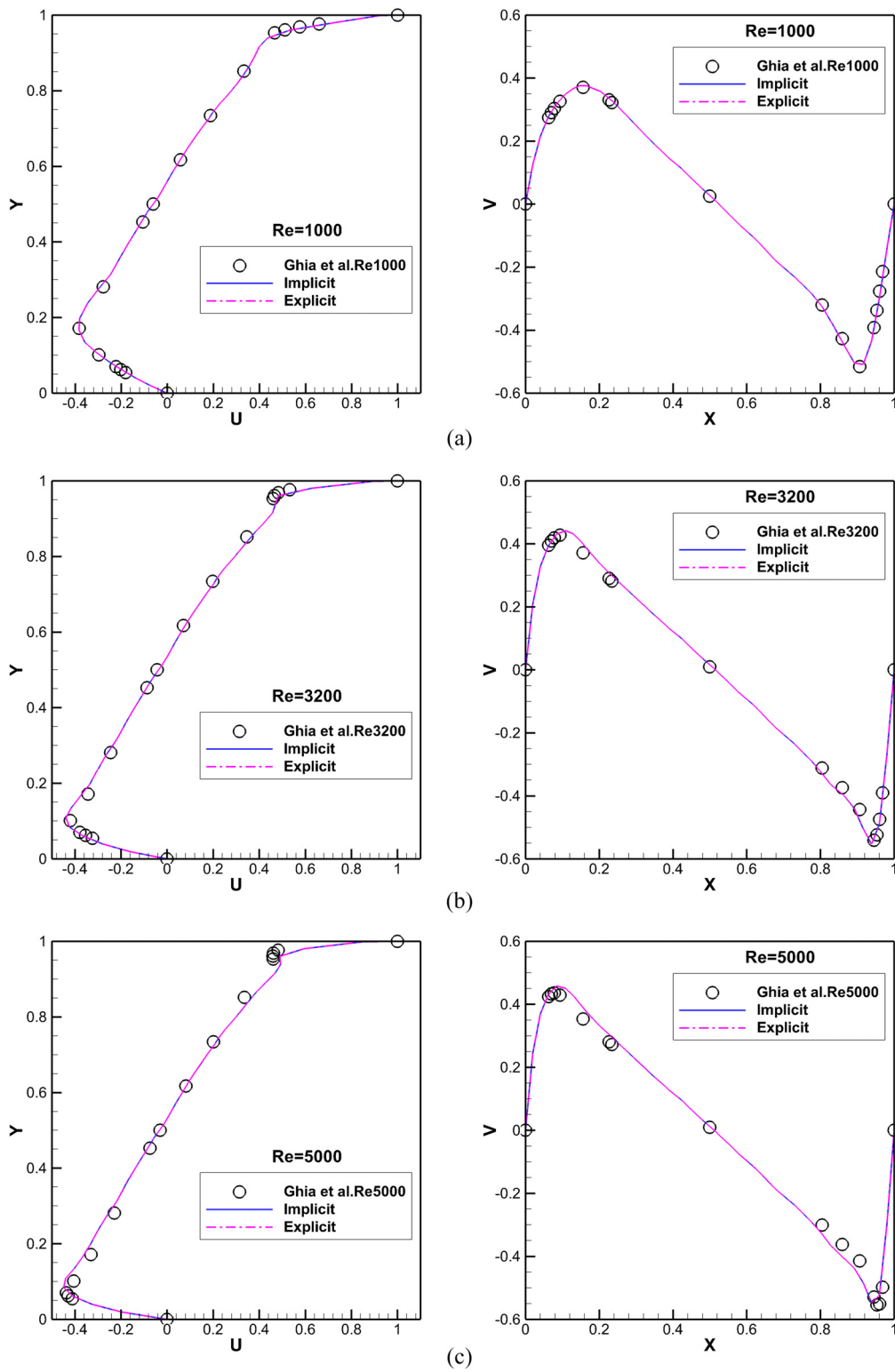


FIG. 6. Comparison of u -velocity (left) and v -velocity (right) profiles along vertical and horizontal central lines of different temporal discretization methods for 2D lid-driven cavity flow at (a) $Re = 1000$, (b) $Re = 3200$, and (c) $Re = 5000$ on the mesh of 2734 cells.

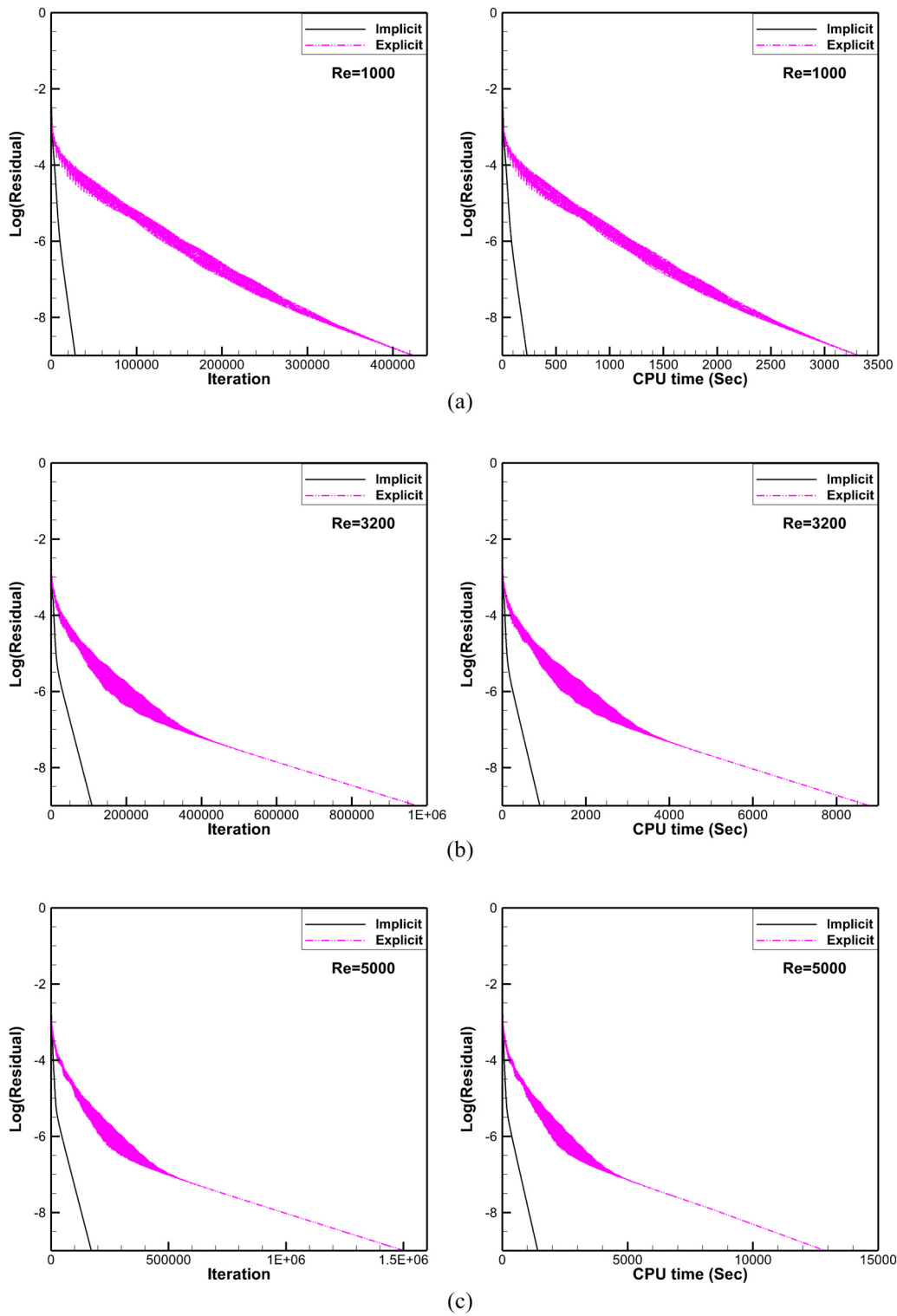


FIG. 7. Comparison of convergence history (left) and CPU time (right) of different temporal discretization methods for 2D lid-driven cavity flow at (a) $Re = 1000$, (b) $Re = 3200$, and (c) $Re = 5000$ on the mesh of 2734 cells.

TABLE VI. Comparison of the CPU time between the explicit and implicit methods for lid-driven cavity flow.

Reynolds numbers	Explicit method		Implicit method		Speedup
	Iteration steps	CPU time (s)	Iteration steps	CPU time (s)	
1000	423 685	3 310.6	28 279	229.3	14.4
3200	974 911	8 800.0	108 857	898.1	9.8
5000	1 504 234	12 897.1	171 322	1411.6	9.1

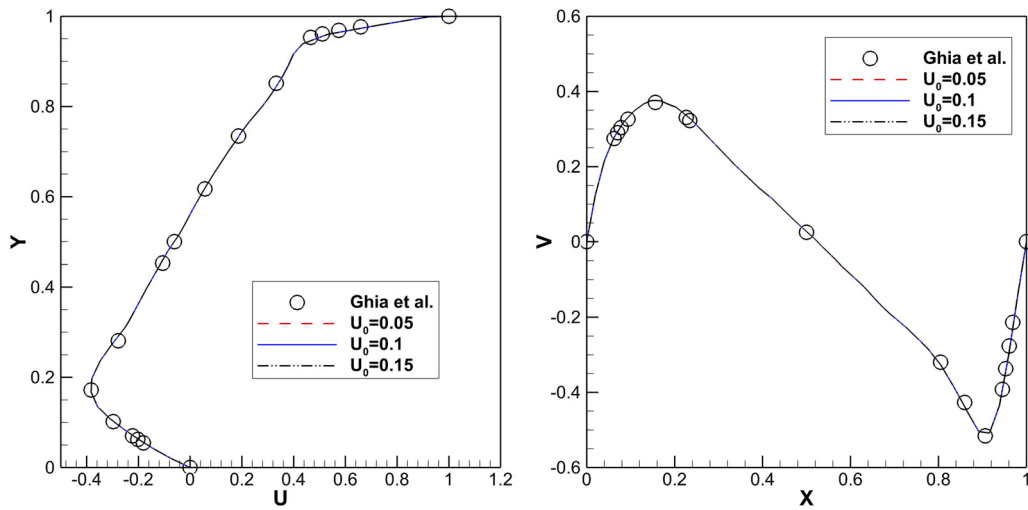


FIG. 8. Comparison of u -velocity (left) and v -velocity (right) profiles along vertical and horizontal central lines of different lid velocities for 2D lid-driven cavity flow at $Re = 1000$ on the mesh of 2734 cells. (a) Velocity profiles along the central lines. (b) Convergence history.

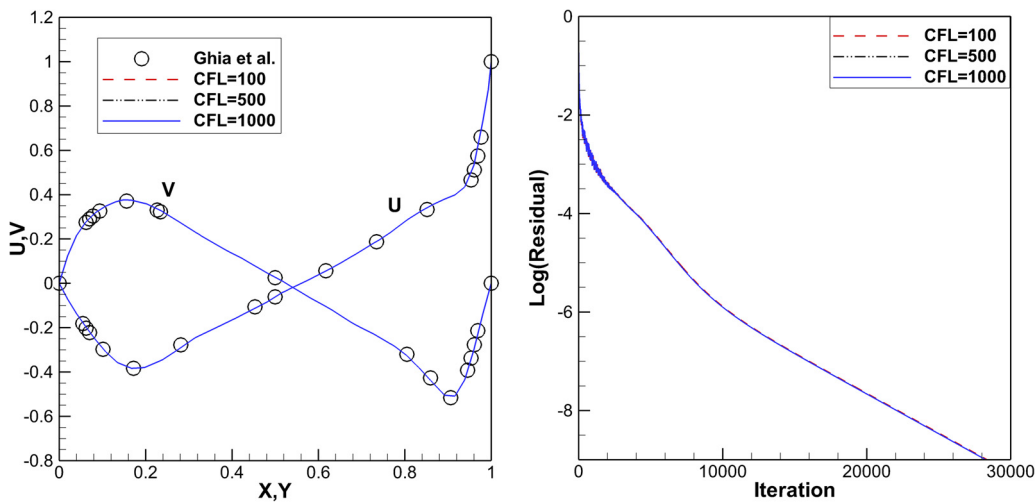


FIG. 9. Comparison of (a) velocity profiles along the central lines and (b) convergence history of different CFL numbers for 2D lid-driven cavity flow at $Re = 1000$ on the mesh of 2734 cells.

Furthermore, the effects of the Mach number and time step are also investigated in this classical problem. Since the dimensionless Mach number is defined by $Ma = U_0/c_s$, where the sound speed c_s is $1/\sqrt{3}$ as introduced in Sec. II A, the different velocities of the moving lid correspond to different Mach numbers. In addition, the time step in the implicit temporal discretization for this steady case is determined by the CFL number. Thus, different time steps would be taken if different CFL numbers are chosen. Specifically, three sets of lid velocity, i.e., $U_0 = 0.05, 0.1, \text{ and } 0.15$

corresponding to the Mach numbers $Ma \approx 0.087, 0.173, \text{ and } 0.260$ which are all within the low Mach number limit ($Ma < 0.3$), are tested. Meanwhile, three CFL numbers of 100, 500, and 1000 are used to determine the effect of the time step. All these comparative investigations are conducted at $Re = 1000$ on the mesh shown in Fig. 5.

The computed results of different velocities U_0 are compared in Fig. 8. Clearly, these results are consistent and they all agree well with the reference data. This outcome confirms that, within the low Mach

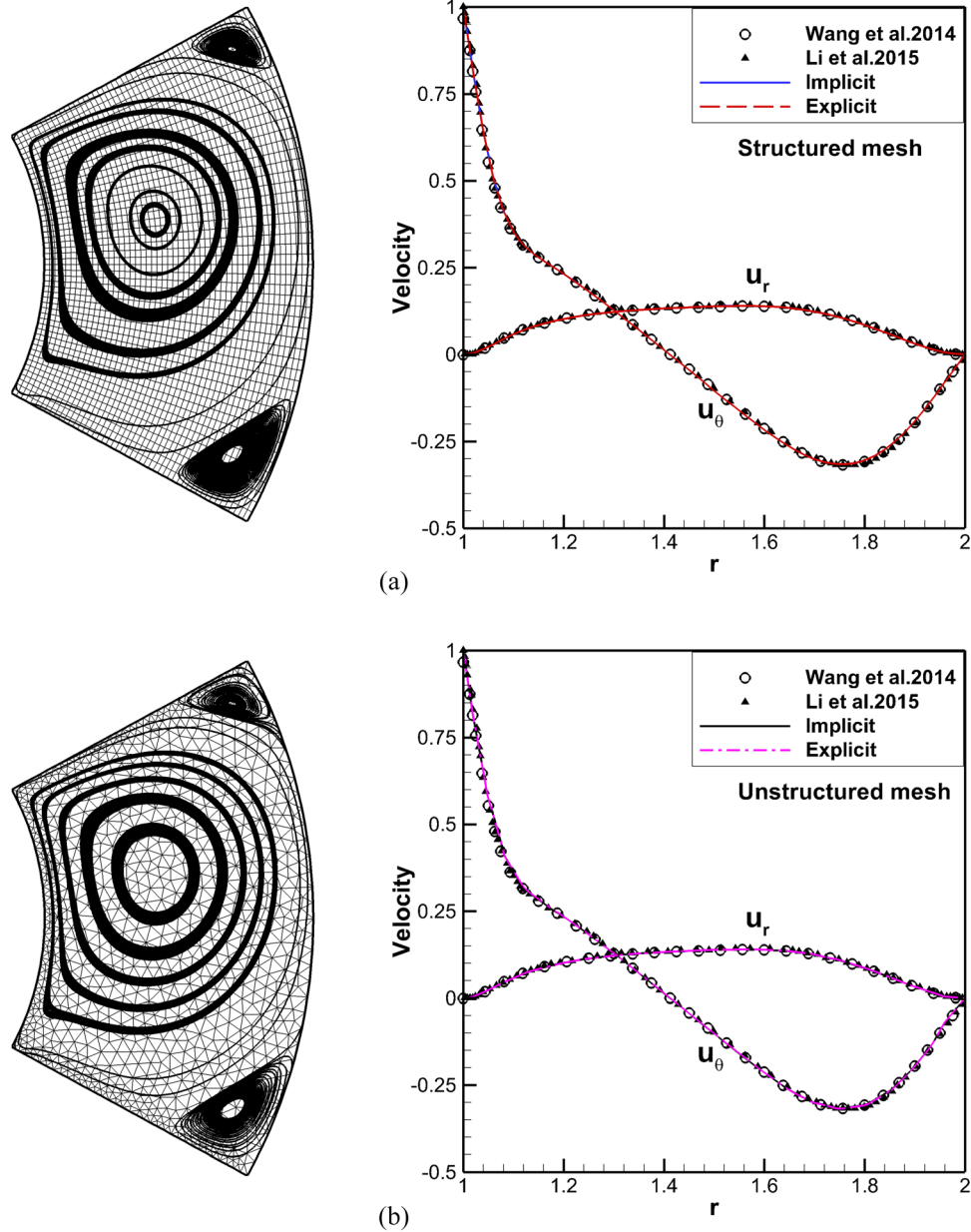


FIG. 10. Streamlines (left) and comparison of velocity distributions along radial and azimuthal directions of different temporal discretization methods (right) for polar cavity flow at $Re = 350$ on the (a) uniform quadrilateral mesh and (b) unstructured triangular mesh.

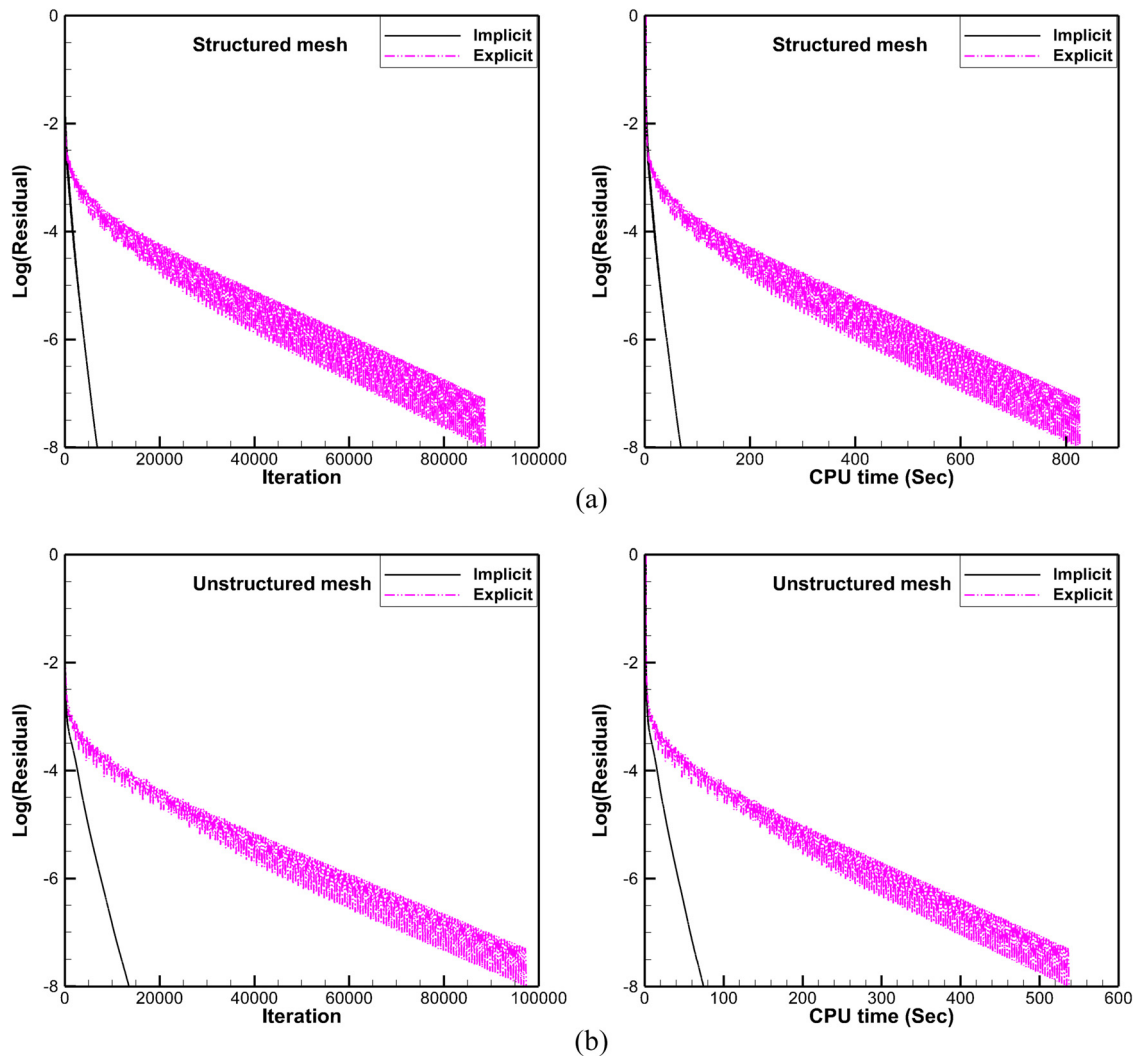


FIG. 11. Comparison of convergence history (left) and CPU time (right) of different temporal discretization methods for polar cavity flow at $Re = 350$ on the (a) uniform quadrilateral mesh and (b) unstructured triangular mesh.

number limit, the Mach number does not affect the accuracy of the solution. Figure 9 compares the results obtained with different time steps. Basically, the same results in good accordance with the benchmark data are obtained, which reveals the independence of the solution precision from the time step. Additionally, the comparison of the

convergence history using different time steps in Fig. 9 further verifies that the computational efficiency remains high when a large time step is used. However, no significant improvement of the convergence rate would be achieved with the CFL number increased when the CFL number is large enough (e.g., $CFL = 100$).

TABLE VII. Comparison of the CPU time between the explicit and implicit methods for Polar cavity flow.

	Cells of mesh	Explicit method		Implicit method		Speedup
		Iteration steps	CPU time (s)	Iteration steps	CPU time (s)	
Structured mesh	2500	88 657	824.2	6841	66.7	12.4
Unstructured mesh	1790	97 339	535.8	13 540	73.3	7.3

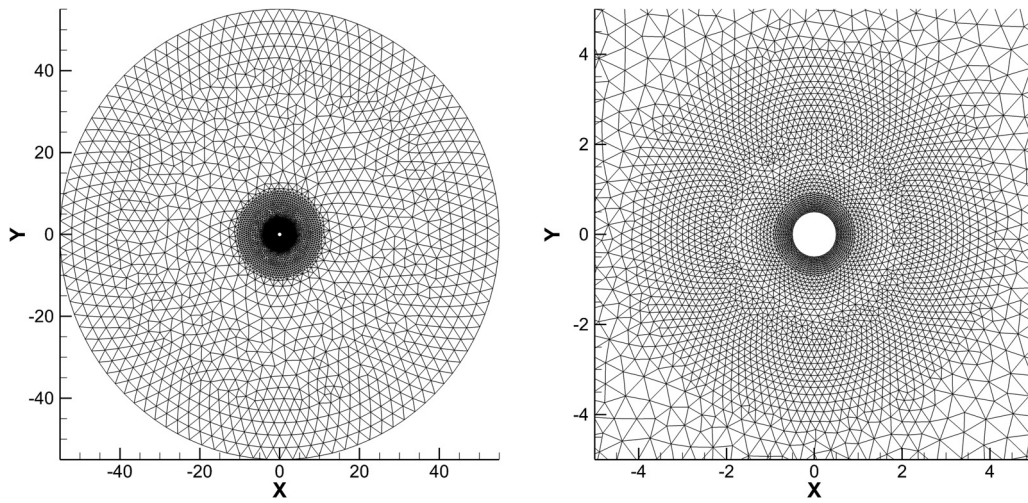


FIG. 12. Unstructured mesh (left) and its partial view (right) for the viscous flow past a circular cylinder. 65 grid points on the cylinder; 11 626 cells.

D. Polar cavity flow on unstructured mesh

To further examine the accuracy and efficiency of the present ILSFD-FV method for the incompressible flow problem with curved boundary, the lid-driven flow in a polar cavity is carried out. Its physical configuration is that a sector with the angle of one radian ($\theta = 1$) is bounded by two straight walls and two curved walls at the radius of R_i and R_o .³⁹ The flow pattern is governed by the non-dimensional Reynolds number defined as $Re = U_\theta(R_o - R_i)/\nu$, where U_θ is the azimuthal velocity on the inner curved wall with radius of R_i . In this simulation, $R_i = 1.0$, $R_o = 2.0$, and $U_\theta = 0.1$. Since the boundaries are curved in this problem, for comparison purposes, two grids are used. One is the unstructured mesh which has 1790 triangle cells and 35 points on each side of the flow domain. The other is the structured one which has the 51×51 uniform grids.

Figure 10 depicts the comparison of streamlines and velocity distributions along radial and azimuthal directions at $Re = 350$ with the

uniform structured mesh and unstructured triangular mesh. The numerical results obtained by the high-order LSFDFV method coupled with the explicit method and the implicit method are validated by the data from Wang *et al.*³⁹ and Tavakoli *et al.*⁵² It is evidently proven that the ILSFD-FV method on the structured mesh or the unstructured mesh can be applied to solve the problems with the curved boundary. Furthermore, from the comparison of the convergence history in Fig. 11 and the comparison of the iteration steps and the CPU time used in Table VII, it is clear that the implicit method is more efficient than the explicit one. The corresponding speedup ratio is from 7 to 12.

E. Viscous flow past a stationary circular cylinder on unstructured meshes

To further demonstrate the capability of the present high-order ILSFD-FV method for solving steady flow problems with curved

TABLE VIII. Comparison of drag coefficients, recirculation lengths, and separation angles for steady flow past a stationary circular cylinder at $Re = 20$ and 40.

Re	References	C_d	L_s/D	$\theta_s Z$	Iteration steps	CPU time (s)
20	Dennis and Chang ⁵⁵	2.05	0.94	43.7		
	Shukla <i>et al.</i> ⁵⁶	2.07	0.92	43.3		
	Pellerin <i>et al.</i> ⁵⁴	2.003	0.92	43.32		
	Explicit method	2.003	0.911	43.31	143 922	6 905.3
	Implicit method	2.073	0.92	43.69	11 462	451.5
	Speedup					15.3
40	He and Doolen ⁵⁸	1.499	2.245	52.84		
	Pellerin <i>et al.</i> ⁵⁴	1.502	2.260	53.29		
	Shu <i>et al.</i> ³⁸	1.53	2.24	52.69		
	Explicit method	1.511	2.242	52.56	120 794	5 258.8
	Implicit method	1.509	2.247	53.13	6166	233.2
	Speedup					22.6

boundary and the performance of the ESDIRK method adopted for the unsteady flow problems, validation on the viscous flow past a stationary circular cylinder⁵³ is conducted at various Reynolds numbers ($Re = 20, 40, \text{ and } 100$). Physically, the configuration of this problem is the uniform incoming viscous fluid flowing over a stationary circular cylinder. The flow pattern of this case is characterized by the Reynolds number $Re = U_0L/\nu$, where L is the diameter of the circular cylinder. To satisfy the incompressible limit, the free-stream velocity is chosen as $U_0 = 0.1$. The lift coefficient C_l , drag coefficient C_d , and Strouhal number S_t are useful parameters and commonly used to check the accuracy of numerical results. They are defined as

$$C_l = \frac{F_l}{\rho_0 U_0^2/2}, \quad C_d = \frac{F_d}{\rho_0 U_0^2/2}, \quad S_t = \frac{f_q L}{U_0}, \quad (39)$$

where ρ_0 denotes the free-stream density, F_l denotes the lift force, F_d represents the drag force, and f_q is the vortex shedding frequency. Furthermore, the geometrical quantities of the eddies, such as the recirculation length L_s and the separation angle θ_s , are also measured for steady flows.

For the steady simulation of $Re = 20, 40$ and the unsteady simulation of $Re = 100$, an unstructured mesh (see Fig. 12) with 65 grid points on the cylinder wall and 11 626 cells in total is used with the far-field boundary at $55L$ away from the center of the cylinder. For quantitative comparison, the drag coefficient C_d , the length of the recirculation zone L_s , the separation angle θ_s , and the CPU time used for the implicit method and the explicit method in steady cases are tabulated and compared with the reference data,^{38,54–58} as shown in Table VIII. In this table, it is clear that the present results are in good agreement with the reference data, which further validates the

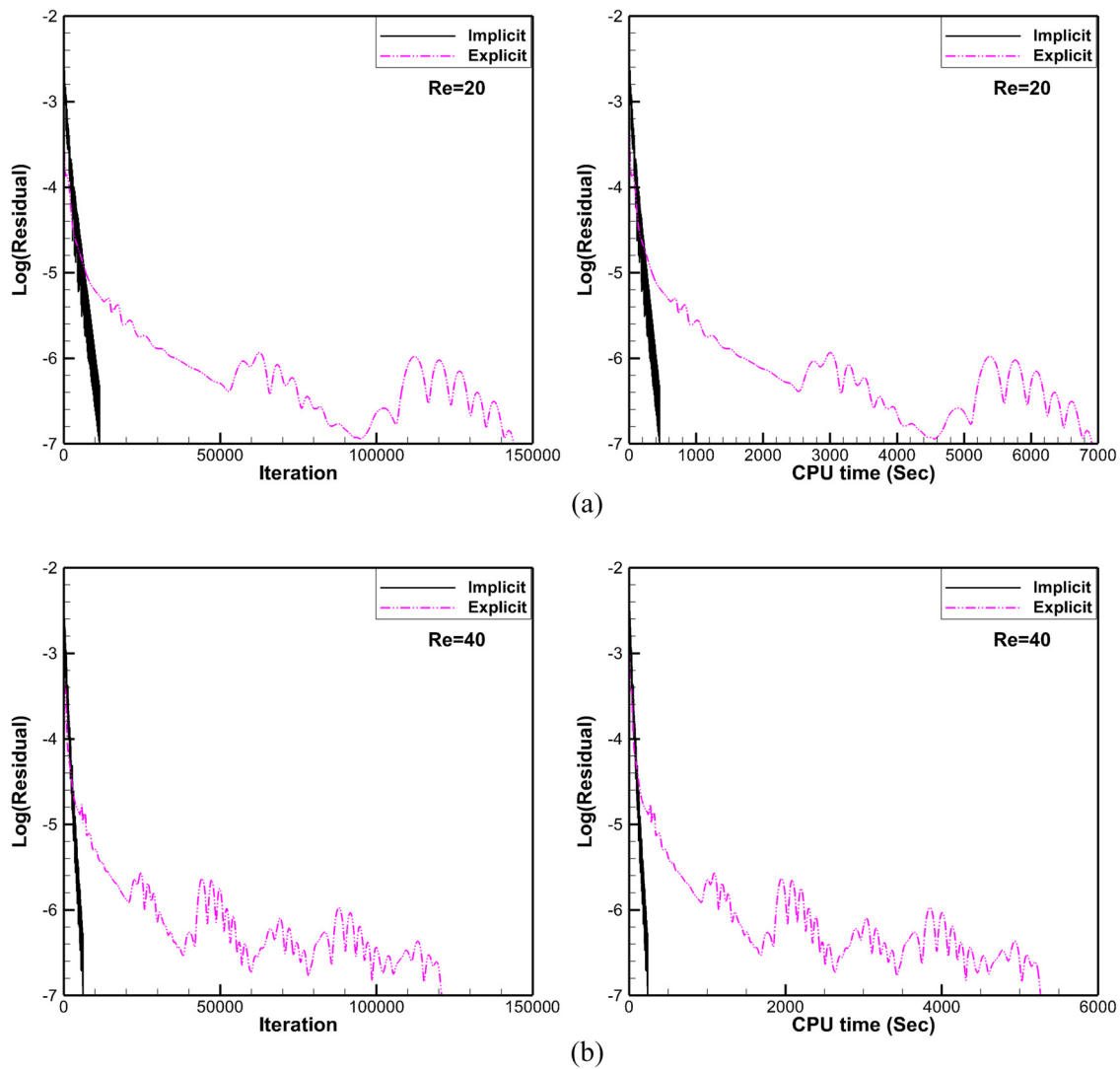


FIG. 13. Comparison of convergence history (left) and CPU time (right) of different temporal discretization methods for steady viscous flow around cylinder at (a) $Re = 20$ and (b) $Re = 40$.

TABLE IX. Comparison of dynamic parameters for unsteady flow past a stationary circular cylinder at $Re = 100$.

Re	References	C_l	C_d	S_t	Iteration steps	CPU time (s)
100	Braza <i>et al.</i> ⁵⁹	± 0.30	1.28 ± 0.02	0.16		
	Liu <i>et al.</i> ⁶⁰	± 0.339	1.350 ± 0.02	0.164		
	Shu <i>et al.</i> ³⁸	± 0.33	1.334 ± 0.02	0.164		
	Pellerin <i>et al.</i> ⁵⁴	± 0.325	1.325	0.164		
	Explicit method	± 0.326	1.322 ± 0.013	0.164	1 000 000	149 554.0
	Implicit method	± 0.324	1.322 ± 0.013	0.164	5000	24 038.2
	Speedup					6.2

accuracy and the ability of the present high-order ILSFD-FV method in solving the steady flow problems with curved boundaries. Furthermore, the comparisons of convergence history of the implicit method and the explicit method for steady simulation at $Re = 20$ and 40 are presented in Fig. 13. Such outcomes in Table VIII and Fig. 13 indicate that the ILSFD-FV method is more efficient and the implicit method can provide more than one order of magnitude improvement in the computation time. For the unsteady case at $Re = 100$, the calculations perform until $t = 500$. The time step for the explicit scheme is $\Delta t = 0.0005$ and the physical time step for the implicit scheme is chosen as a constant $\Delta t = 0.1$. The CFL number for the local pseudo time step is 5. The comparisons of dynamic parameters against the reference data^{38,54,59,60} are presented in Table IX. Additionally, the evolution of the lift and drag coefficient of the explicit method and the implicit method for the unsteady flow problem at $Re = 100$ is shown in Fig. 14. Moreover, Fig. 15 depicts the comparisons of the evolution of the lift and drag coefficients for these two different methods. As can be seen, on the same mesh, the results of ILSFD-FV method and the explicit one are all within the range of reference data and the implicit one outperforms the explicit one in terms of the computation time used. In addition, it is noteworthy that the mesh used in this test is coarser than ones in previous implementation^{38,54} with the second-order of accuracy while comparable results are obtained. These

validate the accuracy, efficiency, and the flexibility on unstructured grids of the present high-order ILSFD-FV method for solving the unsteady flow problems with curved boundaries.

IV. CONCLUSIONS

This paper presents an efficient high-order implicit least squares-based finite difference-finite volume method on arbitrary grids for incompressible flow simulation. The essence of this method lies in the effective combination of the efficient implicit time integration algorithms and the high-order spatial LSFV method which has an implicit nature. By introducing the implicit LU-SGS and ESDIRK schemes to the high-order LSFV method, the convergence speed is accelerated greatly and the computation effort is reduced significantly.

This space-time high-order method has been validated by representative steady and unsteady benchmark cases, including decaying vortex flow, plane Poiseuille flow, lid-driven cavity flow, polar cavity flow, and flow past a stationary circular cylinder. Numerical results evidently prove the high-order of accuracy and high computational efficiency of the developed method as well as its capability of handling unstructured mesh. Compared with the explicit counterpart, the implicit one has the better computational efficiency. As such, this

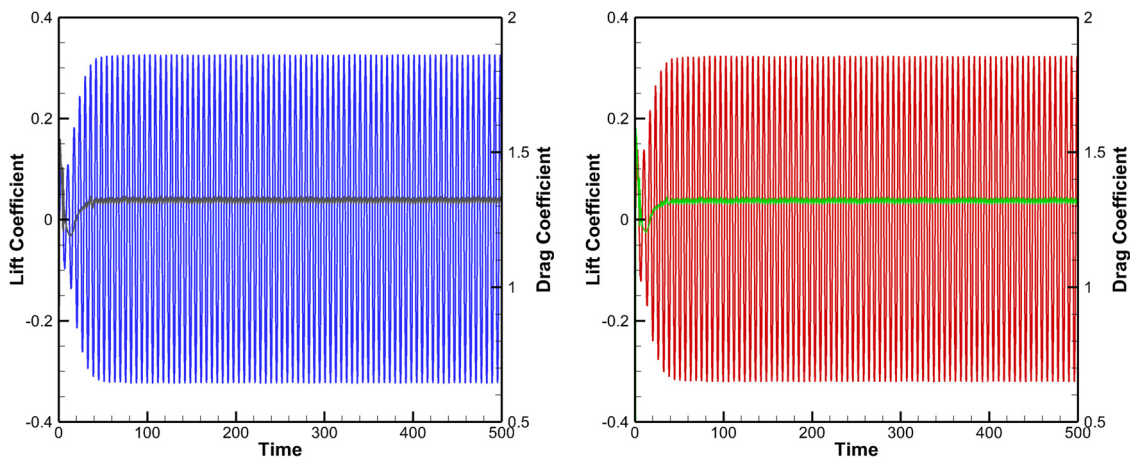


FIG. 14. Evolution of the lift and drag coefficients computed by the explicit method (left) and the implicit method (right) for the flow past a cylinder at $Re = 100$.

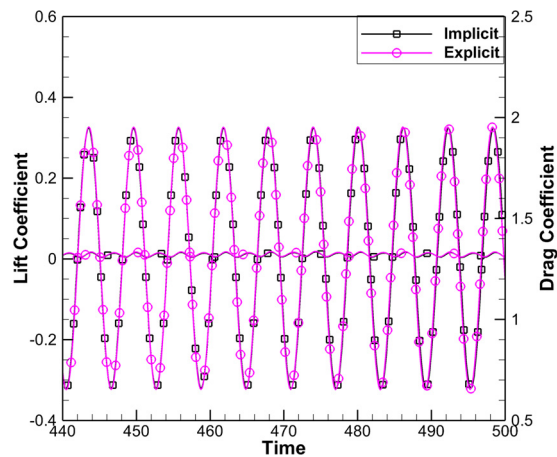


FIG. 15. Comparison of the evolution of the lift and drag coefficients computed by the explicit method and the implicit method for the flow past a cylinder at $Re = 100$.

high-order ILSFD-FV method may provide a promising way to solve practical problems of engineering interest.

ACKNOWLEDGMENTS

The research is partially supported by the Ministry of Education (MOE) of Singapore and the National Numerical Wind Tunnel Project of China (Grant No. NNW2019ZT2-B28).

DATA AVAILABILITY

The data that support the findings of this study are available within the article.

REFERENCES

- ¹T. J. Barth, "Recent developments in high-order k-exact reconstruction on unstructured meshes," AIAA Paper No. 93-0668, 1993.
- ²T. J. Barth, "Aspects of unstructured grids and finite-volume solvers for the Euler and Navier–Stokes equations," AGARD Report No. 787, 1992.
- ³Q. Wang, Y. X. Ren, and W. Li, "Compact high order finite volume method on unstructured grids II: Extension to two-dimensional Euler equations," *J. Comput. Phys.* **314**, 883–908 (2016).
- ⁴Q. Wang, Y. X. Ren, J. Pan, and W. Li, "Compact high order finite volume method on unstructured grids III: Variational reconstruction," *J. Comput. Phys.* **337**, 1–26 (2017).
- ⁵O. Friedrich, "Weighted essentially non-oscillatory schemes for the interpolation of mean values on unstructured grids," *J. Comput. Phys.* **144**, 194–212 (1998).
- ⁶C. F. Ollivier-Gooch, "Quasi-ENO schemes for unstructured meshes based on unlimited data-dependent least-square reconstruction," *J. Comput. Phys.* **133**, 6–17 (1997).
- ⁷R. Abgrall, "On essentially non-oscillatory schemes on unstructured meshes: Analysis and implementation," *J. Comput. Phys.* **114**, 45–58 (1994).
- ⁸C. Hu and C. W. Shu, "Weighted essentially non-oscillatory schemes on triangular meshes," *J. Comput. Phys.* **150**, 97–127 (1999).
- ⁹R. Abgrall, "An essentially non-oscillatory reconstruction procedure on finite-element type meshes: Application to compressible flows," *Comput. Methods Appl. Mech. Eng.* **116**, 95–101 (1994).
- ¹⁰F. Bassi and S. Rebay, "A higher-order accurate discontinuous finite element method for the numerical solution of the compressible Navier–Stokes equations," *J. Comput. Phys.* **131**, 267–279 (1997).

- ¹¹F. Bassi and S. Rebay, "A higher-order accurate discontinuous finite element solution of the 2D Euler equations," *J. Comput. Phys.* **138**, 251–285 (1997).
- ¹²B. Cockburn and C. W. Shu, "The Runge–Kutta discontinuous Galerkin method for conservation laws V: Multidimensional system," *J. Comput. Phys.* **141**, 199–224 (1998).
- ¹³J. Qiu and C. W. Shu, "Hermite WENO schemes and their application as limiters for Runge–Kutta discontinuous Galerkin method: One-dimensional case," *J. Comput. Phys.* **193**, 115–135 (2004).
- ¹⁴J. Zhu, J. Qiu, C. W. Shu, and M. Dumbser, "Runge–Kutta discontinuous Galerkin method using WENO limiters II: Unstructured meshes," *J. Comput. Phys.* **227**, 4330–4353 (2008).
- ¹⁵J. Zhu, X. Zhong, C. W. Shu, and J. Qiu, "Runge–Kutta discontinuous Galerkin method using a new type of WENO limiters on unstructured meshes," *J. Comput. Phys.* **248**, 200–220 (2013).
- ¹⁶R. Hartmann, "Numerical analysis of higher order discontinuous Galerkin finite element methods," in *VKI Lecture Series*, edited by H. Deconinck (Von Karman Institute for Fluid Dynamics, RhodeSaint Genèse, Belgium, 2008), Vol. 8, pp. 13–17.
- ¹⁷Z. J. Wang, Y. Liu, G. May, and A. Jameson, "Spectral difference method for unstructured grids II: Extension to the Euler equations," *J. Sci. Comput.* **32**, 45–71 (2007).
- ¹⁸C. Ma, J. Wu, and T. Zhang, "A high order spectral difference-based phase field lattice Boltzmann method for incompressible two-phase flows," *Phys. Fluids* **32**, 122113 (2020).
- ¹⁹Z. J. Wang and Y. Liu, "Spectral (finite) volume method for conservation laws on unstructured grids II: Extension to two dimensional scalar equation," *J. Comput. Phys.* **179**, 665–697 (2002).
- ²⁰Z. J. Wang and Y. Liu, "Spectral (finite) volume method for conservation laws on unstructured grids III: One-dimensional systems and partition optimization," *J. Sci. Comput.* **20**, 137–157 (2004).
- ²¹Z. J. Wang and Y. Liu, "Spectral (finite) volume method for conservation laws on unstructured grids IV: Extension to two dimensional systems," *J. Comput. Phys.* **194**, 716–741 (2004).
- ²²Y. Sun, Z. J. Wang, and Y. Liu, "Spectral (finite) volume method for conservation laws on unstructured grids VI: Extension to viscous flow," *J. Comput. Phys.* **215**, 41–58 (2006).
- ²³Z. J. Wang, "Spectral (finite) volume method for conservation laws on unstructured grids: Basic formulation," *J. Comput. Phys.* **178**, 210–251 (2002).
- ²⁴Z. J. Wang and H. Gao, "A unifying lifting collocation penalty formulation including the discontinuous Galerkin, spectral volume/difference methods for conservation laws on mixed grids," *J. Comput. Phys.* **228**, 8161–8186 (2009).
- ²⁵H. Gao and Z. J. Wang, "A conservative correction procedure via reconstruction formulation with the chain-rule divergence evaluation," *J. Comput. Phys.* **232**, 7–13 (2013).
- ²⁶T. J. Barth and P. Frederickson, "Higher order solution of the Euler equations on unstructured grids using quadratic reconstruction," in 28th Aerospace Sciences Meeting, Paper No. 90-0013 (1990).
- ²⁷Y. Y. Liu, C. Shu, H. W. Zhang, and L. M. Yang, "A high order least square-based finite difference-finite volume method with lattice Boltzmann flux solver for simulation of incompressible flows on unstructured grids," *J. Comput. Phys.* **401**, 109019 (2019).
- ²⁸H. Luo, J. D. Baum, and R. Löhner, "A fast, matrix-free implicit method for compressible flows on unstructured grids," *J. Comput. Phys.* **146**, 664–690 (1998).
- ²⁹M. Cheng, G. Wang, and H. H. Mian, "Reordering of hybrid unstructured grids for an implicit Navier–Stokes solver based on openMP parallelization," *Comput. Fluids* **110**, 245–253 (2015).
- ³⁰R. F. Chen and Z. J. Wang, "An improved LU-SGS scheme with faster convergence for unstructured grids of arbitrary topology," AIAA Paper No. 99-0935, 1999.
- ³¹A. Jameson, "Time dependent calculations using multigrid with applications to unsteady flows past airfoils and wings," AIAA Paper No. 1991-1596, 1991.
- ³²C. Cox, C. Liang, and M. W. Plesniak, "A high-order solver for unsteady incompressible Navier–Stokes equations using the flux reconstruction method on unstructured grids with implicit dual time stepping," *J. Comput. Phys.* **314**, 414–435 (2016).
- ³³H. Bijl, M. H. Carpenter, V. N. Vatsa, and C. A. Kennedy, "Implicit time integration schemes for the unsteady compressible Navier–Stokes equations: Laminar flow," *J. Comput. Phys.* **179**, 313–329 (2002).

- ³⁴V. Kazemi-Kamyab, A. H. van Zuijlen, and H. Bijl, "Analysis and application of high order implicit Runge–Kutta schemes to collocated finite volume discretization of the incompressible Navier–Stokes equations," *Comput. Fluids* **108**, 107–115 (2015).
- ³⁵Y. Xia, X. Liu, H. Luo, and R. Nourgaliev, "A third-order implicit discontinuous Galerkin method based on a Hermite WENO reconstruction for time-accurate solution of the compressible Navier–Stokes equations," *Int. J. Numer. Methods Fluids* **79**, 416–435 (2015).
- ³⁶H. Ding, C. Shu, and K. S. Yeo, "Development of least square-based two-dimensional finite difference schemes and their application to simulate natural convection in a cavity," *Comput. Fluids* **33**, 137–154 (2004).
- ³⁷H. Ding, C. Shu, K. S. Yeo, and D. Xu, "Simulation of incompressible viscous flows past a circular cylinder by hybrid FD scheme and meshless least square-based finite difference method," *Comput. Methods Appl. Mech. Eng.* **193**, 727–744 (2004).
- ³⁸C. Shu, Y. Wang, C. J. Teo, and J. Wu, "Development of lattice Boltzmann flux solver for simulation of incompressible flows," *Adv. Appl. Math. Mech.* **6**, 436–460 (2014).
- ³⁹Y. Wang, C. Shu, and C. J. Teo, "Development of LBGK and incompressible LBGK-based lattice Boltzmann flux solvers for simulation of incompressible flows," *Int. J. Numer. Methods Fluids* **75**, 344–364 (2014).
- ⁴⁰J. M. Pérez, A. Aguilar, and V. Theofilis, "Lattice Boltzmann methods for global linear instability analysis," *Theor. Comput. Fluid Dyn.* **31**, 643–664 (2017).
- ⁴¹S. Hou, Q. Zou, S. Chen, G. Doolen, and A. C. Cogley, "Simulation of cavity flow by the lattice Boltzmann method," *J. Comput. Phys.* **118**, 329–347 (1995).
- ⁴²X. He and L. S. Luo, "Lattice Boltzmann model for the incompressible Navier–Stokes equation," *J. Stat. Phys.* **88**, 927–944 (1997).
- ⁴³Z. Chen, C. Shu, L. M. Yang, X. Zhao, and N. Y. Liu, "Immersed boundary-simplified thermal lattice Boltzmann method for incompressible thermal flows," *Phys. Fluids* **32**, 013605 (2020).
- ⁴⁴B. Harikrishnan, Z. Chen, and C. Shu, "A new explicit immersed boundary method for simulation of fluid–solid interactions," *Adv. Appl. Math. Mech.* **13**, 261–284 (2021).
- ⁴⁵L. M. Yang, C. Shu, W. M. Yang, and Y. Wang, "A simplified circular function-based gas kinetic scheme for simulation of incompressible flows," *Int. J. Numer. Methods Fluids* **85**, 583–598 (2017).
- ⁴⁶L. M. Yang, C. Shu, Z. Chen, Y. Y. Liu, Y. Wang, and X. Shen, "High-order gas kinetic flux solver for simulation of two dimensional incompressible flows," *Phys. Fluids* **33**, 017107 (2021).
- ⁴⁷Z. Chen, C. Shu, Y. Wang, L. M. Yang, and D. Tan, "A simplified lattice Boltzmann method without evolution of distribution function," *Adv. Appl. Math. Mech.* **9**, 1–22 (2017).
- ⁴⁸Y. Sun, C. Shu, C. J. Teo, Y. Wang, and L. M. Yang, "Explicit formulations of gas-kinetic flux solver for simulation of incompressible and compressible viscous flows," *J. Comput. Phys.* **300**, 492–519 (2015).
- ⁴⁹L. Q. Zhang, Z. Chen, L. M. Yang, and C. Shu, "An improved discrete gas-kinetic scheme for two-dimensional viscous incompressible and compressible flows," *Phys. Fluids* **31**, 066103 (2019).
- ⁵⁰Z. Chen, C. Shu, and D. Tan, "Highly accurate simplified lattice Boltzmann method," *Phys. Fluids* **30**, 103605 (2018).
- ⁵¹U. Ghia, K. N. Ghia, and C. T. Shin, "High-Re solutions for incompressible flow using the Navier–Stokes equations and a multigrid method," *J. Comput. Phys.* **48**, 387–411 (1982).
- ⁵²E. Tavakoli, B. Lessani, and R. Hosseini, "High-order pole-treatment in cylindrical coordinates for incompressible flow simulations with finite-difference collocated schemes," *J. Comput. Phys.* **296**, 1–24 (2015).
- ⁵³J. Wang and C. Zhou, "A novel immersed boundary method implemented by imposing reconstructed velocity on virtual boundary," *Adv. Appl. Math. Mech.* **13**, 83–100 (2021).
- ⁵⁴N. Pellerin, S. Leclaire, and M. Reggio, "Solving incompressible fluid flows on unstructured meshes with the lattice Boltzmann flux solver," *Eng. Appl. Comput. Fluid Mech.* **11**, 310–327 (2017).
- ⁵⁵S. C. R. Dennis and G. Z. Chang, "Numerical solutions for steady flow past a circular cylinder at Reynolds numbers up to 100," *J. Fluid Mech.* **42**, 471–489 (1970).
- ⁵⁶R. K. Shukla, M. Tatineni, and X. Zhong, "Very high-order compact finite difference schemes on non-uniform grids for incompressible Navier–Stokes equations," *J. Comput. Phys.* **224**, 1064–1094 (2007).
- ⁵⁷J. Wu and C. Shu, "Implicit velocity correction-based immersed boundary-lattice Boltzmann method and its applications," *J. Comput. Phys.* **228**, 1963–1979 (2009).
- ⁵⁸X. He and G. Doolen, "Lattice Boltzmann method on curvilinear coordinates system: Flow around a circular cylinder," *J. Comput. Phys.* **134**, 306–315 (1997).
- ⁵⁹M. Braza, P. Chassaing, and H. H. Minh, "Numerical study and physical analysis of the pressure and velocity fields in the near wake of a circular cylinder," *J. Fluid Mech.* **165**, 79–130 (1986).
- ⁶⁰C. Liu, X. Zheng, and C. H. Sung, "Preconditioned multigrid methods for unsteady incompressible flows," *J. Comput. Phys.* **139**, 35–57 (1998).